Turkish Journal of Earth Sciences

Volume 30 | Number 2 Article 3

1-1-2021

Multiple fluid-mineral equilibria approach to constrain the evolution of thermal watersin the Hisaralan geothermal field, Simav Graben, western Turkey

ALİ GÖKGÖZ

HALİM MUTLU

MEHMET ÖZKUL

ALİ KAMİL YÜKSEL

TÜBİTAK

Turkish Journal of Earth Sciences

http://journals.tubitak.gov.tr/earth/

Research Article

Turkish J Earth Sci
(2021) 30: 182-203

doi:10.3906/yer-2007-14

Multiple fluid-mineral equilibria approach to constrain the evolution of thermal waters in the Hisaralan geothermal field, Simav Graben, western Turkey

Ali GÖKGÖZ[1,*], Halim MUTLU[2], Mehmet ÖZKUL[1], Ali Kamil YÜKSEL[3]

[1]Department of Geological Engineering, Engineering Faculty, Pamukkale University, Denizli, Turkey
[2]Department of Geological Engineering, Engineering Faculty, Ankara University, Ankara, Turkey
[3]Department of Geological Engineering, Engineering Faculty, Balıkesir University, Balıkesir, Turkey

Received: 12.07.2020 • **Accepted/Published Online:** 19.11.2020 • **Final Version:** 22.03.2021

Abstract: In this study seasonal changes in the geochemical and stable isotope compositions of Hisaralan thermal waters in Simav Graben, western Turkey, were investigated with regards to a variety of mineral-water interactions and mixing processes. The Hisaralan and Emendere geothermal waters, with temperatures of up to 99 °C, were mostly of Na-HCO_3 and Ca-HCO_3 types. The $\delta^{18}O$ and $\delta^{2}H$ values of the Hisaralan waters ranged from –9.32‰ to –8.73‰ and –65.02‰ to –61.10‰, with maximum seasonal differences of 0.3‰ and 1.8‰. The Emendere waters were represented by a more positive range of $\delta^{2}H$ values (–54.95‰ to –54.61‰), while their $\delta^{18}O$ compositions (–9.04 to –8.41‰) were very similar to those of the Hisaralan waters. The stable isotope compositions of the Hisaralan thermal waters were consistent with those of the global meteoric water line, whereas the Emendere waters closely resembled those of the Marmara meteoric water line. The $\delta^{13}C$ of the dissolved inorganic carbon varied from –4.33‰ to –2.77‰ for the thermal waters and from –13.84‰ to –12.51‰ for the cold waters. These values indicated a marine carbonate origin for the former and an organic source for the latter. Sulfur isotope systematics of dissolved sulfate in the Hisaralan geothermal waters indicated that the sulfate was most likely derived from the dissolution of marine carbonates and terrestrial evaporites. Chemical geothermometers applied to the Hisaralan thermal waters yielded average reservoir temperatures of 123 to 152 °C, which were rather consistent with those estimated using the silica-enthalpy (146 to 154 °C) and chloride-enthalpy (142 to 178 °C) mixing models. The recharge elevations of the thermal waters that were computed from the $\delta^{2}H$ compositions were between 1060 and 1330 m.

Key words: Geochemistry, stable isotopes, geothermometer, Hisaralan geothermal field, Turkey

1. Introduction

The ongoing N-S extension in western Anatolia has resulted in the formation of several graben systems since the Late Oligocene (Yılmaz et al., 2000; Lips et al., 2001; Çemen et al., 2006; Van Hinsbergen, 2010; Jolivet et al., 2013; Ersoy et al., 2014). Almost all of the geothermal power plants in Turkey have been installed in these grabens, namely Simav, Gediz, Büyük Menderes, and Küçük Menderes, from north to south. Among them, the WNW-ESE-extending Simav Graben, which has a length of about 150 km, hosts not only high geothermal potential, but also a variety of epithermal ore deposits (e.g., Oygür, 1997; Yılmaz et al., 2013). There is a good record of tectonism, volcanism, and hydrothermal activity around the graben, which manifests itself as the occurrence of numerous high-temperature hot springs (Mutlu and Güleç, 1998; Karakuş, 2015), and modern and fossil alteration zones, where various industrial deposits, including alunite (Mutlu et al., 2005) and kaolin (Ece et al., 2013), are mined. Thermal waters in this graben are manifested along the Simav Fault (Baba and Sözbilir, 2012; Bundschuh et al., 2013), which is a north-dipping normal fault that has been active since the Late Miocene (Seyitoğlu, 1997a). The major geothermal fields extending from east to west along the Simav Graben (e.g., Abide-Gediz, Simav, and Hisaralan) are shown in Figure 1a, with their respective discharge temperatures and total dissolved solids (TDSs) values (in mg/L). Extensive drilling in the graben over the last 30 years has ascertained bottom-hole temperatures over 160 °C (Burçak et al., 2013). Fluids in these geothermal fields have relatively different temperature and TDS values, and chemical composition (Figure 1a).

The Hisaralan and Emendere geothermal fields are located in NW part of the Simav Graben, nearly 20 km east and 5 km southeast of the town of Sındırgı in the city of Balıkesir, respectively (Figure 1a). In Hisaralan, there are nearly 70 thermal springs, most of which are issued from pools of about 1 m across, but some are manifested from

* Correspondence: agokgoz@pau.edu.tr

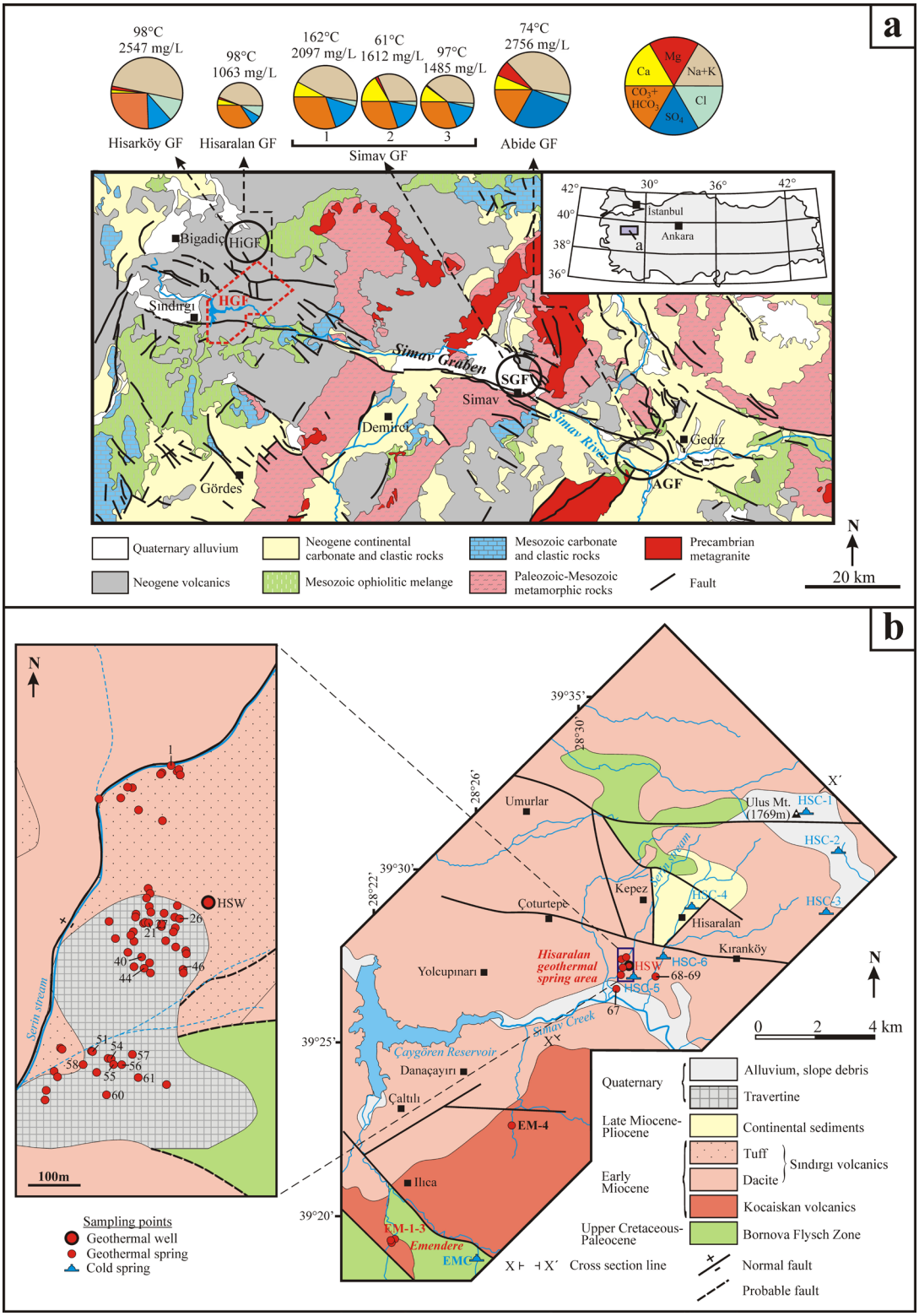

Figure 1. a) Geology map of Simav Graben with major geothermal fields (simplified from Konak, 2002; Emre et al., 2011; chemical compositions of thermal waters were taken from Gemici and Tarcan, 2007 for the Bigadiç geothermal field, Karakuş, 2015 for the Simav geothermal field, Akkuş et al., 2005 for the Abide geothermal field). b) Geology map of the Hisaralan and Emendere geothermal areas with the water sample locations (modified from Erkül et al., 2006).

travertine mounds and towers up to 2 m and 5 m in height, respectively. Several springs also exist within the perennial stream beds. Hisaralan thermal waters with a total discharge of at least 86 L/s are used for spa and greenhouse (total area of 4943 m^2) heating and balneological purposes. In the area, the Turkish Petroleum Corporation (Ankara, Turkey) drilled an exploration well to a depth of 881 m, which produced water at a temperature of 106 °C and discharge of 32 L/s. Waters from this well are currently used for house heating (for a total of 1300 residences in the town of Sındırgı) and thermal baths.

In this study, geochemical characteristics, and processes affecting the chemistry and mineral equilibrium of the thermal waters in the Hisaralan and neighboring Emendere geothermal fields were investigated pertaining to a variety of mineral-water interaction and mixing mechanisms. Water chemistry and stable isotope compositions (oxygen, hydrogen, carbon, and sulfur) of the waters and dissolved constituents were used to determine the source of the thermal fluids and predict the reservoir temperatures. The current findings will provide new insights into the sources and mechanisms of the mineral-water interaction processes in high-temperature geothermal systems in the Hisaralan area, western Turkey.

2. Materials and methods

In order to examine seasonal differences in the physicochemical parameters, the waters from the Hisaralan and Emendere geothermal fields were sampled during both wet and dry periods in 2016. In April, 18 thermal and 5 cold water samples were collected and in October, 18 thermal and 6 cold water samples were collected. During the field campaign in October 2017, 4 thermal and 1 cold water samples were collected. With the exception of water from the Hisaralan geothermal well (HSW), all of the other water samples were collected from springs or pools. Temperature, electrical conductivity (EC), and pH of thermal and cold waters were measured at the sampling localities using a Hach Lange HQ40D multimeter (Loveland, CO, USA). Before the measurements were taken, the device was calibrated with standard solutions.

For the major ion, oxygen isotope ($\delta^{18}O$)-hydrogen isotope ($\delta^{2}H$), and tritium (^{3}H) analyses, samples were collected into double-plugged 250-mL, 50-mL, and 500-mL high-density polyethylene (HDPE) containers by filtering (0.45 μm), and kept cold until analyzed. For the element analysis, samples were collected into 100-mL HDPE bottles by filtering, and ultrapure HNO_3 was added until it reached a pH of 2 or below. Samples for the SiO_2 analysis were collected into 100-mL containers by diluting with ultrapure water. For the carbon isotope ($\delta^{13}C$) [dissolved inorganic carbon (DIC)] analysis, water samples were collected into double-plugged 100-mL containers, and kept cold until analysis. For analysis of the sulfur isotope ($\delta^{34}S$) and $\delta^{18}O$ of the dissolved sulfate, samples were collected into containers of varying volumes (100 to 2000 mL), depending on the sulfate content, and filtered, and then diluted ultrapure HCl was added to keep the pH at 4–5. Next, 100 to 150 mg of $BaCl_2.2H_2O$ was added to the water samples to precipitate $BaSO_4$.

The major ion and ^{3}H analyses of the water samples were performed at the laboratories of Hacettepe University using ion chromatography and the liquid scintillation counting method, respectively. The CO_3 and HCO_3 concentrations were determined using H_2SO_4 titration. Silica analysis was performed at the Geochemistry Laboratory of Pamukkale University via spectrophotometry. Trace element analysis was performed at Acme Laboratories (Vancouver, Canada) via inductively-coupled plasma mass spectrometry, with detection limit varying from 0.01 to 5 ppb depending on the element of interest. The total charge balance errors were within ± 4%.

$\delta^{18}O$ and $\delta^{2}H$ analyses were conducted at the SIRFER Laboratory of the University of Utah using a Picarro cavity ring-down spectrometer (Santa Clara, CA, USA) with an analytical precision of 0.1‰ Vienna Standard Mean Ocean Water (VSMOW) for $\delta^{18}O$ and 0.2‰ VSMOW for $\delta^{2}H$. The $\delta^{34}S$ Canyon Diablo Troilite (CDT) and $\delta^{18}O$ (VSMOW) of the dissolved sulfate and $\delta^{13}C$ Vienna Pee Dee Belemnite (VPDB) of the dissolved inorganic carbon (DIC) were analyzed via elemental analyzer isotope ratio mass spectrometry (EA-IRMS) at the Environmental Isotope Laboratory of the University of Waterloo, Canada. Results for these analyses were reported at a 2-sigma error range with precision of about 0.2%.

3. Geological and hydrogeological setting

Since the Late Oligocene, western Anatolia has undergone deformation that has resulted in the formation of NE-trending basins over the basement rocks of the Menderes Massif, Sakarya Zone, and Bornova Flysch Zone (Seyitoğlu and Scott, 1994; Seyitoğlu, 1997b; Yılmaz et al., 2000; Bozkurt, 2003). The Neogene-Quaternary volcanism, contemporaneous with the development of these basins, is represented chiefly by lava flows, domes, and pyroclastics that were distributed throughout the region (Erkül et al., 2006). The metamorphic core complexes in western Anatolia exhumed as a result of late Cenozoic continental extension. The ongoing exhumation of the Menderes Massif in the south of study area is controlled by the Simav Fault (Figure 1a). The Simav Fault, with a length of 56 km, extending between the districts of Soma and Afyon, is a segment of the Sındırgı-Sincanlı Fault Zone of right-lateral strike-slip character (Seyitoğlu et al., 2004).

The basement in the Hisaralan and the Emendere areas is represented by the Bornova Flysch Zone (Figure

1b), which is a regional olistostrome-mélange belt, ca. 60 km wide and 225 km long, located between the İzmir-Ankara Tethyan suture in the northwest and the Menderes Massif in the southeast (Okay et al., 2012). The zone, which was first described by Brinkmann (1971), contains a matrix of Maastrichtian-Danian-aged neritic limestone blocks exceeding 20 km in size (Erdoğan and Güngör, 1992; Okay and Altıner, 2007; Okay et al., 2012). The basement rocks are overlain by the Kocaiskan and Sındırgı volcanics of Early Miocene age (Figure 1b) (Erkül et al., 2005). The Kocaiskan volcanics, which are exposed only in the Emendere area, are composed of andesitic lavas and pyroclastic rocks that yielded a K-Ar age of 23.2 Ma (Erkül et al., 2005). The unit is unconformably covered by the Sındırgı volcanics, which consist of lavas of dacite and rhyolite composition that passes upward into pyroclastics. The pyroclastic unit contains medium- to coarse-grained, subrounded-subangular radiolarite and ultramafic rock fragments cemented in a dark red-green matrix. The age of the Sındırgı volcanics spans from 18.9 to 19.8 Ma (Yılmaz et al., 2013). The late Miocene-Pliocene continental deposits are made up of fluvial sediments interlayered with red and cream-colored sandstone and conglomerate beds (Figure 1b). This intercalating sequence is composed chiefly of volcanic and nonvolcanic clasts. The clasts are composed of well-rounded and moderately lithified sandstone, limestone, quartzite, various volcanic rock fragments, and trace amounts of metamorphic and granite clasts within a sandy-silty matrix (Erkül et al., 2005). The quaternary travertines were formed in association with horst-graben structures and NE-SW-trending oblique faults that are genetically linked to the normal fault systems (e.g., the Simav Fault), which have been active since the neotectonic period.

Intensely cracked and jointed neritic limestones of the Bornova Flysch zone are the main reservoir rocks in the Hisaralan geothermal area. In addition to this, fractured zones in the volcanic rocks comprise the secondary reservoir. The marbles, schists (especially calc-schist and quartz-schist), and quartzites of the Menderes Massif form a deep geothermal reservoir. A static temperature test conducted in the HSW revealed 2 different production zones (Aksoy et al., 2009). The temperature in the shallow production zone, at depths of 0–50 m, increased up to 98 °C, and then decreased down to 200 m, and then increased once again. The maximum temperature in the second production zone, at 550–675 m, was 107 °C. According to these findings by Aksoy et al. (2009), geothermal fluids in the Hisaralan field are discharged from both shallow and deep units (500–700 m).

In the Hisaralan area, the cap rocks are not sufficiently impervious and thick to keep the reservoir hot and prevent the fluid loss. However, less permeable tuffs, volcanic units, and argillised ultramafic rocks at the altered zones may act as cap rocks. The impermeable lithologies of the ophiolitic rocks overlying the recrystallised limestone can also be considered as cap rocks.

The Hisaralan geothermal field is located in a tectonically active region. Recent earthquakes have been the manifestation of seismic unrest in the province. For example, the 15 October 1942 Bigadiç earthquake, with a magnitude of 6.2, occurred at a distance of only 20 km from the study area (Atabey, 2000). Active faults, intense seismicity, and thermal springs in the vicinity of the Hisaralan area indicate that tectonism in the region is still active. Moreover, the region is represented by a significantly high heat flow (164 mW m^{-2}; İlkışık, 1995). The geothermal gradient map based on the estimation of the Curie point depths (CPDs) of western Turkey has shown that the geothermal gradient is about 70 °C/km for the Sındırgı region (Bilim et al., 2016). A high geothermal gradient closely associated with a cooling magma at depth is thought to be the major heat source in the Hisaralan field.

The Hisaralan geothermal field is recharged by meteoric waters infiltrating mainly from the volcanic rocks, which are widely exposed on the Ulus mountain and surrounding areas in the northeast. The NNW-SSE-trending faults and fracture sets are the major conduits for the emergence of thermal waters at the surface (Figure 2).

4. Results

4.1. Water chemistry

Water samples from the Hisaralan and Emendere fields were collected during field campaigns in April and October 2016, and October 2017 (Tables 1 and 2). EC and pH values of the sampled waters were 1175 to 1493 µS/cm and 6.87 to 8.13 for April and 1193 to 1643 µS/cm and 6.39 to 8.08 for October. The pH values of the unsampled waters varied from 6.10 to 8.78. Although the EC and pH of waters with temperatures >90 °C did not significantly vary seasonally, those of some low-temperature springs increased in October (e.g., temperatures increased from 74.0 to 80.2 °C for sample HS-27 and from 75.1 to 88.1 °C for sample HS-54, from 78.0 to 84.1 °C for sample HS-58 and from 54.5 to 59.3 °C for sample HS-69). This might indicate that reservoir pressure was increased in the dry period and the rate of mixing with cold groundwater was limited, which was also supported by the increasing EC values in October. Regarding the Emendere field, temperatures of the hot waters varied from 25.2 to 32.0 °C, the EC values were between 266 and 436 µS/cm, and the pH was in the range of 7.08 to 8.89.

Cations and anions in most of the Hisaralan thermal waters followed the order of Na>Ca>K>Mg and HCO_3>Cl>SO_4 (in meq/L), indicating the dominance of

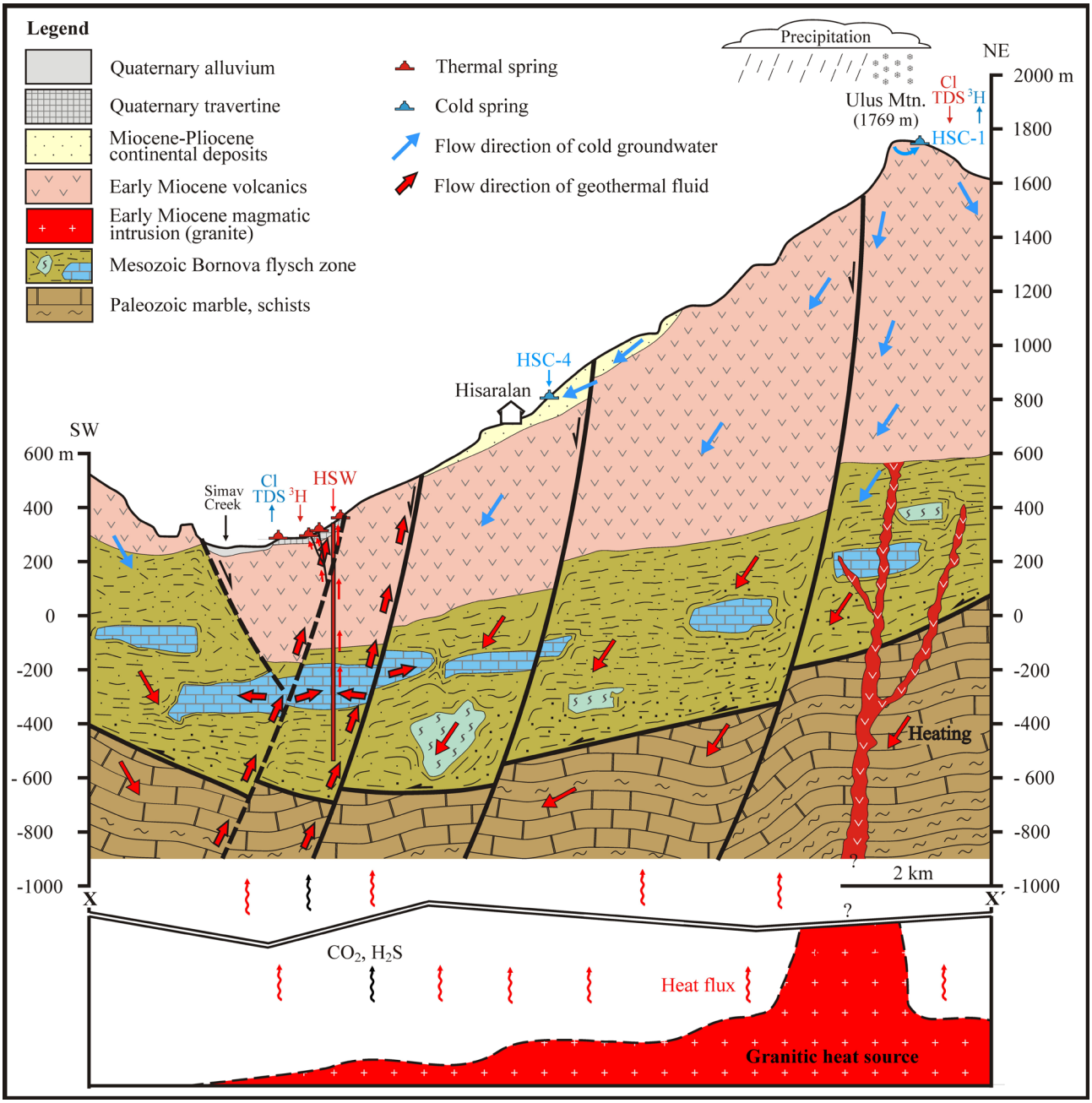

Figure 2. Hydrogeological conceptual model of the Hisaralan geothermal field.

Na-HCO_3-type water. However, the cold waters were Ca-HCO_3-type waters. The thermal waters in the Emendere field were represented by Ca-Mg-HCO_3-type water.

The Na concentrations of the thermal waters in the Hisaralan area were 230 to 294 mg/L (average 269 mg/L) and 243 to 336 mg/L (average 289 mg/L) for April and October 2016, respectively. The SiO_2 varied from 92 to 122 mg/L (average 111 mg/L) and 107 to 155 mg/L (average 133 mg/L) for the respective seasons, indicating an increase in the dry period. Unlike the Na and SiO_2 contents, the average HCO_3 concentrations of the waters during these periods remained almost unchanged, at 548 mg/L and 549 mg/L. This was also the case for Ca, with average concentrations of 25.2 and 25.3 mg/L. Regarding the Emendere waters, 4 thermal springs were investigated, of which only 1 sample (EM-3) was reanalyzed (Table 1). The TDS contents of these waters varied from 223 to 384 mg/L, which were significantly lower than those of the Hisaralan samples (928 to 1192 mg/L).

Table 1. Results of the chemical analysis of the studied waters sampled in April 2016 (concentrations in mg/L; EC: μS/cm; HSW: Hisaralan geothermal well, HS: Hisaralan thermal spring, HSC: Hisaralan cold spring, EM: Emendere thermal spring).

Area	No	T(°C)	EC	pH	Na	K	Ca	Mg	CO_3	HCO_3	Cl	SO_4	F	B	Li	Sr	Br	NO_3	SiO_2	CBE[a] (%)	Water type
Hisaralan	HSW	97.0	1493	7.62	285.5	18.4	24.4	3.5	36	524.6	86.6	96.0	9.23	5.072	1.039	0.459	0.187	0.16	117.0	−0.64	Na-HCO_3
	HS-1	93.2	1422	7.07	271.3	17.4	23.5	3.0	54	469.7	84.4	94.5	8.79	4.660	0.977	0.428	0.270	0.17	108.4	−1.81	Na-HCO_3
	HS-21	85.6	1433	7.24	272.7	17.2	22.1	2.9	12	524.6	86.7	98.9	9.55	4.934	0.979	0.481	0.316	0.30	114.6	−0.81	Na-HCO_3
	HS-26	97.0	1380	8.13	293.5	18.2	12.4	2.2	36	475.8	87.8	97.3	9.52	5.082	1.044	0.401	0.327	0.22	121.5	0.62	Na-HCO_3
	HS-27	74.0	1397	7.12	278.6	17.6	25.8	3.4	12	555.1	80.5	95.9	9.28	4.886	1.004	0.541	0.184	0.07	114.6	0.08	Na-HCO_3
	HS-40	73.6	1403	7.15	268.6	17.1	24.5	3.3	12	524.6	80.7	95.5	9.13	4.738	0.946	0.514	0.245	0.17	109.7	−0.00	Na-HCO_3
	HS-44	95.1	1427	7.74	275.7	17.5	18.2	2.6	15	512.4	85.2	94.6	9.10	4.940	1.019	0.467	0.333	0.30	117.2	−0.19	Na-HCO_3
	HS-46	93.0	1422	7.26	285.6	18.1	19.2	2.6	12	542.9	84.1	98.5	9.80	4.918	1.018	0.467	0.321	0.52	113.6	−0.17	Na-HCO_3
	HS-51	95.7	1429	7.17	273.7	17.6	21.2	3.6	0	573.4	80.2	94.2	8.85	4.812	0.988	0.506	0.209	0.10	113.4	−0.90	Na-HCO_3
	HS-54	75.1	1283	6.91	239.9	15.9	34.7	4.1	0	549.0	74.0	91.2	7.75	4.316	0.854	0.586	0.265	0.78	101.5	−1.43	Na-HCO_3
	HS-57	87.9	1442	6.97	275.3	17.7	20.6	3.2	0	567.3	82.4	114.4	8.89	4.926	0.988	0.500	0.210	0.09	112.1	−2.19	Na-HCO_3
	HS-58	78.0	1418	7.14	273.8	17.5	22.1	3.9	0	567.3	81.7	97.3	8.66	4.604	0.968	0.553	0.345	0.19	110.8	−0.61	Na-HCO_3
	HS-60	77.6	1432	7.19	288.7	18.4	18.4	3.4	0	585.6	84.4	108.2	9.20	4.902	1.035	0.513	0.240	0.14	116.7	−1.17	Na-HCO_3
	HS-61	96.4	1466	7.19	269.0	18.1	25.3	4.5	0	573.4	79.7	92.7	8.75	5.046	1.017	0.482	0.172	0.16	120.3	−0.35	Na-HCO_3
	HS-67	54.1	1445	6.87	266.6	14.8	50.5	4.8	18	640.5	78.1	95.2	6.19	4.520	0.899	0.821	0.276	0.21	94.3	−1.94	Na-HCO_3
	HS-68	69.8	1273	7.01	241.2	10.6	34.3	3.1	0	567.3	64.2	76.1	6.24	3.744	0.765	0.656	0.221	0.20	100.7	−0.72	Na-HCO_3
	HS-69	54.5	1175	6.93	229.5	9.2	32.5	1.9	0	555.1	61.2	72.4	5.83	3.402	0.693	0.715	0.240	0.47	91.7	−2.23	Na-HCO_3
	HSC-1	4.6	54	8.35	2.6	0.7	9.0	0.8	0	24.4	2.0	6.6	0.02	0.007	0.001	0.012	0.014	0.00	4.7	4.11	Ca-Na-HCO_3-SO_4
	HSC-2	5.3	62	8.08	2.4	0.7	6.1	4.8	0	36.6	2.6	4.2	0.01	0.010	0.001	0.018	0.011	0.00	9.0	3.80	Mg-Ca-HCO_3
	HSC-3	11.7	80	8.79	5.5	2.7	9.3	2.6	0	30.5	6.1	11.0	0.02	0.011	n.d.	0.063	0.026	0.47	12.0	4.02	Ca-Na-Mg-HCO_3-SO_4
	HSC-4	18.2	360	7.61	12.9	1.4	49.7	9.3	12	176.9	5.1	20.8	0.04	0.010	0.013	0.698	0.029	4.58	17.3	−1.35	Ca-HCO_3
	HSC-5	23.4	724	7.45	40.4	6.0	70.1	28.3	24	311.1	16.4	34.4	0.04	0.028	0.007	1.058	0.053	28.18	35.2	1.32	Ca-Mg-HCO_3
Emendere	EM-3	31.0	428	7.33	4.02	1.05	51.4	21.5	24	219.6	4.5	17.8	0.25	0.027	0.004	0.236	0.048	0.4	14.3	−4.04	Ca-Mg-HCO_3

[a] Charge balance error = ([total cation in meq/L] − [total anion in meq/L]) / ([total cation in meq/L] + [total anion in meq/L]) × 100 (%).
Sample numbers correspond to the locality numbers shown in Figure 1b. n.d.: not detected.

Table 2. Results of the chemical analysis of the studied waters sampled in October 2016 (concentrations in mg/L; EC: µS/cm; EMC: Emendere cold spring).

Area	No	T(°C)	EC	pH	Na	K	Ca	Mg	CO_3	HCO_3	Cl	SO_4	F	B	Li	Sr	Br	NO_3	SiO_2	CBE[a] (%)	Water type
Hisaralan	HSW	98.9	1643	7.60	336.2	21.6	24.4	3.2	54	555.1	84.8	104.4	8.24	6.618	1.353	0.574	0.172	0.07	154.7	2.90	Na-HCO_3
	HS-1	94.0	1463	7.28	285.6	18.4	25.8	3.5	12	555.1	75.9	97.4	6.84	5.886	1.153	0.512	0.166	0.12	131.1	2.12	Na-HCO_3
	HS-21	85.8	1455	7.34	289.5	18.2	23.4	3.0	0	585.6	77.3	101.2	7.02	5.730	1.158	0.536	0.172	0.07	135.7	1.33	Na-HCO_3
	HS-26	96.4	1379	8.08	303.5	19.4	11.7	2.4	48	451.4	79.3	104.7	7.21	6.122	1.200	0.478	0.172	0.08	144.9	3.01	Na-HCO_3
	HS-27	80.2	1430	7.21	295.6	18.6	24.3	3.4	24	549.0	79.6	105.8	7.31	5.744	1.149	0.584	0.166	0.08	134.3	1.22	Na-HCO_3
	HS-40	74.9	1448	7.49	289.3	18.0	23.8	3.2	12	591.7	79.4	102.6	7.14	5.944	1.153	0.552	0.170	0.00	132.1	−0.63	Na-HCO_3
	HS-44	96.3	1428	7.40	287.5	18.5	20.4	2.6	30	512.4	76.2	95.7	6.95	5.730	1.142	0.510	0.162	0.08	136.9	1.66	Na-HCO_3
	HS-46	93.1	1448	7.21	300.6	19.1	25.2	3.1	24	542.9	77.1	103.2	6.93	5.918	1.213	0.565	0.170	0.00	139.8	2.92	Na-HCO_3
	HS-51	96.4	1443	7.27	295.8	18.6	21.0	3.2	0	579.5	76.2	101.4	6.87	5.754	1.183	0.549	0.172	0.09	137.0	2.43	Na-HCO_3
	HS-54	88.1	1412	7.11	274.0	17.5	20.0	4.0	24	506.3	75.6	102.2	6.82	5.712	1.084	0.491	0.166	0.07	131.5	0.48	Na-HCO_3
	HS-55	85.0	1413	7.33	285.3	18.5	21.1	2.3	24	561.2	59.5	87.3	7.08	5.852	1.143	0.448	0.172	0.05	131.0	1.50	Na-HCO_3
	HS-56	93.1	1419	7.91	300.3	18.6	13.6	3.2	24	518.5	78.1	102.6	7.00	5.706	1.146	0.393	0.170	0.09	139.2	2.23	Na-HCO_3
	HS-57	85.1	1444	7.35	291.3	18.2	32.2	3.3	0	573.4	80.1	137.4	6.84	5.756	1.141	0.561	0.176	0.08	138.0	0.99	Na-HCO_3
	HS-58	84.1	1427	6.39	288.9	18.5	19.4	3.9	0	567.3	77.6	104.8	6.94	5.916	1.179	0.543	0.172	0.09	141.5	1.63	Na-HCO_3
	HS-61	95.7	1444	7.40	300.1	18.2	22.3	3.3	12	555.1	80.7	102.0	6.81	5.776	1.125	0.531	0.178	0.07	137.6	2.76	Na-HCO_3
	HS-67	54.7	1450	6.82	275.0	15.0	54.5	5.1	0	664.9	74.0	96.0	4.91	5.106	0.994	0.867	0.156	0.07	107.0	1.25	Na-HCO_3
	HS-68	70.4	1272	7.16	259.7	11.8	35.6	1.7	0	567.3	62.1	78.8	4.92	4.700	0.939	0.816	0.148	0.02	121.9	2.63	Na-HCO_3
	HS-69	59.3	1193	7.59	242.7	9.7	33.9	1.5	30	481.9	53.2	70.5	4.37	3.914	0.793	0.843	0.126	0.35	108.3	2.55	Na-HCO_3
	HSC-1	6.1	86	7.49	3.0	0.7	16.1	0.8	0	48.8	2.3	7.1	0.02	<0.005	0.001	0.021	0.023	0.01	7.8	0.18	Ca-HCO_3
	HSC-2	6.3	96	6.52	3.1	0.9	7.1	6.8	0	48.8	3.4	12.1	0.01	<0.005	0001	0.028	0.032	0.13	10.0	−3.57	Mg-Ca-HCO_3-SO_4
	HSC-3	12.8	82	7.84	5.2	3.1	7.8	1.8	0	30.5	7.3	6.6	0.01	0.005	0.001	0.036	0.052	0.70	15.1	−0.75	Ca-Na-HCO_3-Cl
	HSC-4	18.9	379	7.96	14.5	1.4	54.8	10.4	0	213.5	4.2	20.2	0.07	0.009	0.014	0.799	0.018	3.12	20.7	1.98	Ca-Mg-HCO_3
	HSC-5	20.6	752	7.33	35.5	5.5	84.5	29.4	24	359.9	12.3	31.4	0.09	0.023	0.007	1.133	0.044	24.14	39.1	1.38	Ca-Mg-Na-HCO_3
	HSC-6	16.7	478	7.17	18.9	2.4	76.7	12.9	18	256.2	6.8	22.0	0.07	0.013	0.015	0.696	0.023	8.69	17.0	1.59	Ca-HCO_3
Emendere	EM-1*	30.5	436	7.08	3.8	0.7	59.0	20.8	0	256.2	3.3	15.3	0.26	0.024	0.003	0.216	0.053	0.50	13.3	2.16	Ca-Mg-HCO_3
	EM-2*	28.5	435	8.16	3.5	0.8	58.6	23.5	0	262.3	2.9	18.2	0.20	0.022	0.004	0.236	0.033	0.33	13.9	2.58	Ca-Mg-HCO_3
	EM-3*	32.0	428	7.33	4.0	0.8	63.7	21.3	0	274.5	3.2	15.6	0.25	0.026	0.005	0.237	0.020	0.31	14.8	1.91	Ca-Mg-HCO_3
	EM-4*	25.2	266	8.89	53.8	0.3	15.3	0.6	18	122.0	5.9	6.9	0.15	0.348	0.023	0.018	0.035	0.05	30.2	3.97	Na-Ca-HCO_3
	EMC*	13.0	436	7.64	5.6	0.6	87.0	9.8	0	286.7	3.4	11.8	0.09	0.033	0.006	0.193	0.017	1.46	10.9	3.21	Ca-HCO_3

[a] Charge balance error = ([total cation in meq/L] – [total anion in meq/L]) / ([total cation in meq/L] + [total anion in meq/L]) × 100 (%). *Samples were taken in October 2017. Sample numbers correspond to the locality numbers shown in Figure 1b.

In the Piper diagram (Figure 3a), the Hisaralan samples were plotted on the Na+K and HCO_3 corners, implying that these waters originated from the same reservoir or had undergone the same geochemical process. However, the Emendere thermal waters, except for sample EM-4, were plotted close to the Ca and HCO_3 corners. These waters had a chemical composition that was identical to the Emendere cold waters, which was manifested through ophiolitic rocks (Figures 3a and 3b). This might show that the Emendere thermal waters circulated shallowly with a relatively short residence time (e.g., 1.33 TU). Sample EM-4, which was collected between the Hisaralan and Emendere fields (Figure 1b), was plotted close to the Hisaralan thermal waters. In the semilogarithmic Schoeller diagram (Figure 3b), the chemical composition of this water, although having a low TDS content, likely resembled the Hisaralan thermal waters. Therefore, it was concluded that sample EM-4 was genetically related to the Hisaralan waters and diluted by cold ground waters. In the Piper diagram, the cold waters of both areas fell into the Ca-Mg-HCO_3 field. The chemical composition of the cold waters might have been modified by several factors, including the types of rocks they interacted with, circulation time, and mixing with thermal waters (particularly, sample HSC-5).

4.2. Isotope compositions

4.2.1. Oxygen-hydrogen isotopes

Stable isotopes of hydrogen and oxygen in waters are widely used in geothermal exploration studies to investigate the origin of fluids and assess the physicochemical processes that control hydrologic conditions and fluid character. The $\delta^{18}O$ and $\delta^{2}H$ compositions of the Hisaralan and Emendere waters collected during different seasons are given in Table 3. The $\delta^{18}O$ values of the thermal waters were –9.32‰ to –8.78‰ (VSMOW) for April and –9.24‰ to –8.73‰ (VSMOW) for October 2016. The $\delta^{2}H$ varied from –65.02‰ to –62.29‰ (VSMOW) in April to –63.29‰ to –61.13‰ (VSMOW) in October 2016. The maximum seasonal difference in the $\delta^{2}H$ values of the sample pairs was 1.8‰ and that for $\delta^{18}O$ was only 0.3‰. Regarding the cold waters, the $\delta^{18}O$ values fell in the range of –9.28‰ to –8.30‰ for April and –9.47‰ to –8.28‰ for October 2016. The $\delta^{2}H$ varied from –58.18‰ to –54.12‰ to –58.14‰ to –52.82‰ for these respective periods. The $\delta^{18}O$ and $\delta^{2}H$ compositions of the cold waters varied in a wider range than those of the thermal waters. Moreover, the $\delta^{2}H$ of the cold waters was about 8‰ more positive than that of the thermal water samples (Figure 4). Interestingly, although most of the thermal waters extended parallel to the Global

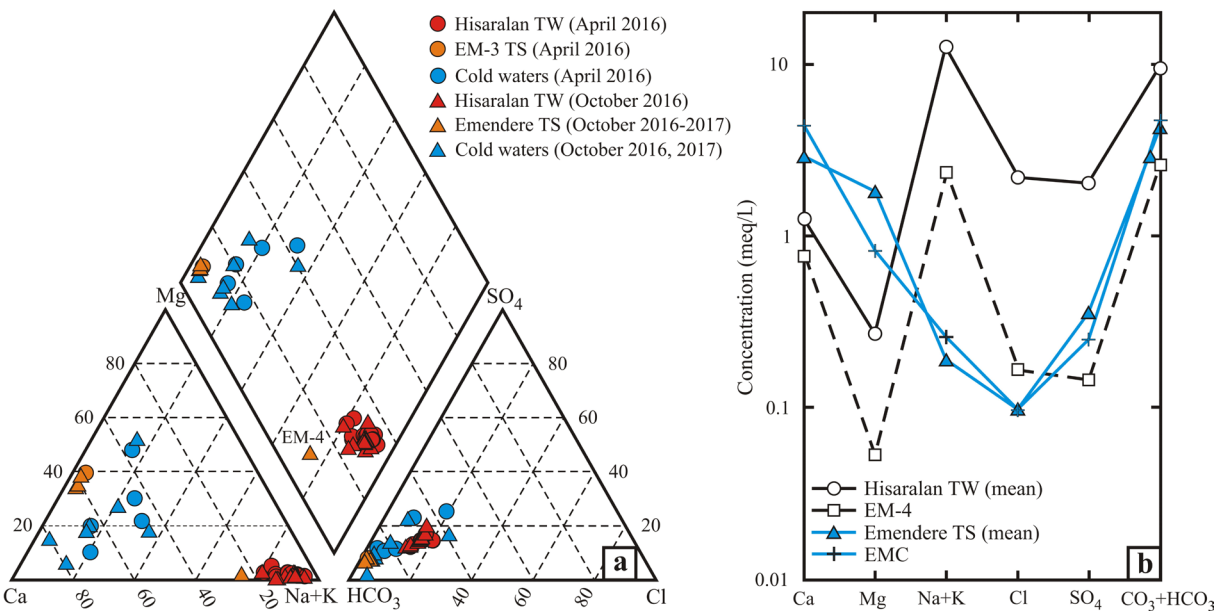

Figure 3. a) Piper and b) semilogarithmic Schoeller diagrams for the Hisaralan and Emendere thermal and cold waters (TW: thermal waters, TS: thermal springs).

Table 3. Results of the stable isotope analysis.

Area	No.	δ^2H	$\delta^{18}O$	d-exc	δ^2H	$\delta^{18}O$	d-exc	Tritium				$\delta^{13}C$ (DIC)	$\delta^{18}O$ (SO_4)	$\delta^{34}S$ (SO_4)
		(VSMOW ‰)						(TU)				(VPDB)	(VSMOW)	(VCDT)
		April 2016			October 2016			April 2016	October 2016	April 2017	November 2017	October 2016		
Hisaralan	HSW	–63.63	–8.99	8.29	–62.24	–8.95	9.36	0.00 ± 0.20	0.54 ± 0.25	-	-	–4.33	0.05	15.97
	HS-1	–65.02	–9.32	9.54	–63.29	–9.24	10.63	0.72 ± 0.22	0.01 ± 0.23	-	-	–2.77	-	-
	HS-21	–64.35	–9.12	8.61	–62.61	–9.04	9.71	-	-	-	-	-	-	-
	HS-26	–63.23	–8.78	7.01	–61.97	–8.73	7.87	0.00 ± 0.21	0.12 ± 0.24	-	-	–3.71	–0.03	15.77
	HS-27	–64.19	–9.10	8.61	–62.58	–9.03	9.66	-	-	-	-	-	-	-
	HS-40	–63.41	–9.00	8.59	–62.00	–8.89	9.12	0.48 ± 0.22	0.45 ± 0.24	-	-	-	-	-
	HS-44	–64.42	–9.11	8.46	-	-	-	0.00 ± 0.23	0.41 ± 0.25	-	-	-	–0.15	15.09
	HS-46	–64.48	–9.12	8.48	–62.82	–9.07	9.74	-	-	-	-	-	-	-
	HS-51	–64.47	–9.16	8.81	–62.85	–9.16	10.43	-	-	-	-	-	-	-
	HS-54	–62.29	–8.93	9.15	–62.89	–9.15	10.31	-	-	-	-	-	-	-
	HS-56	-	-	-	–62.34	–8.91	8.94	-	-	-	-	-	-	-
	HS-57	–64.51	–9.18	8.93	–63.15	–9.17	10.21	0.16 ± 0.21	-	-	-	–3.04	–1.58	13.17
	HS-58	–63.39	–9.00	8.61	–62.41	–8.97	9.35	0.00 ± 0.20	-	-	-	–3.64	–1.17	15.12
	HS-60	–63.46	–8.88	7.58	-	-	-	-	-	-	-	-	-	-
	HS-61	–64.27	–9.15	8.93	–63.08	–9.18	10.36	0.70 ± 0.22	-	-	-	–3.13	–1.15	15.09
	HS-67	–63.08	–8.96	8.60	–61.67	–9.02	10.49	0.08 ± 0.21	-	-	-	-	1.33	15.21
	HS-68	–63.39	–9.01	8.69	–62.16	–9.08	10.48	0.09 ± 0.23	-	-	-	–3.10	–0.05	15.15
	HS-69	–62.42	–8.83	8.22	–61.13	–8.91	10.15	-	-	-	-	-	-	-
	HSC-1	–58.18	–9.28	16.06	–57.49	–9.42	17.87	2.77 ± 0.26	4.03 ± 0.30	-	-	-	-	-
	HSC-2	–57.30	–9.21	16.38	–58.14	–9.47	17.62	-	-	-	-	-	-	
	HSC-3	–57.28	–9.17	16.08	–57.10	–9.37	17.86	2.81 ± 0.26	3.64 ± 0.32	-	-	-	-	-
	HSC-4	–58.01	–9.00	13.99	–56.97	–9.13	16.07	2.64 ± 0.25	4.62 ± 0.34	-	-	–12.51	-	-
	HSC-5	–54.12	–8.30	12.28	–52.82	–8.28	13.42	2.82 ± 0.26	3.38 ± 0.30	-	-	–13.84	-	-
	HSC-6	-	-	-	–55.35	–8.80	15.05	-	2.82 ± 0.29	-	-	-	-	-
	Rainwater	–67.5	–11.1	21.3	–21.70	–3.70	7.90	4.74 ± 0.30	8.21 ± 0.37	6.11 ± 0.36	3.72 ± 0.32	-	-	-
	Snow	-	-	-	–129.4*	–18.4*	17.80	-	-	-	7.34 ± 0.37	-	-	-
Emendere	EM-1	-	-	-	–54.95	–9.00	-	-	-	-	1.32 ± 0.30	-	-	-
	EM-2	-	-	-	–54.67	–8.99	-	-	-	-	-			
	EM-3	-	-	-	–54.75	–9.04	-	-	-	-	1.33 ± 0.28	-	-	-
	EM-4	-	-	-	–54.61	–8.41	-	-	-	-	0.00 ± 0.25	-	-	-
	EMC	-	-	-	–53.78	–8.58	14.86	-	-	-	3.44 ± 0.31	-	-	-

*Sample was taken in October 2017.

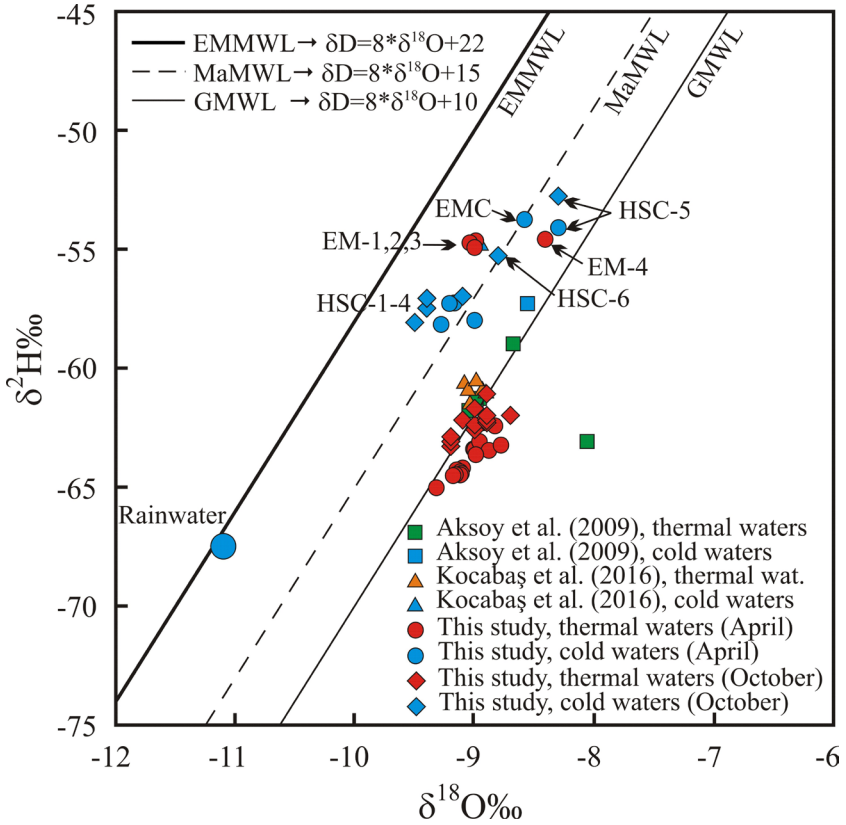

Figure 4. $\delta^{18}O$ vs. $\delta^{2}H$ diagram for the Hisaralan and Emendere thermal and cold waters with stable isotope data from previous studies. Global Meteoric Water Line (GMWL): Craig (1961), Marmara Meteoric Water Line (MaMWL): Yalçın (2007), Eastern Mediterranean Meteoric Water Line (EMMWL): Gat and Carmi (1987).

Meteoric Water Line (GMWL) (Craig, 1961), the cold water samples lay along the Marmara MWL (MaMWL) (Yalçın, 2007).

The Emendere waters exhibited the highest $\delta^{2}H$ values (–54.95 to –53.78‰) among the samples, while their $\delta^{18}O$ compositions (–9.04‰ to –8.41‰) were very similar to those of the Hisaralan samples (Figure 4). The Emendere waters were closely plotted on the MaMWL and implied a different underground flow path when compared to the Hisaralan thermal waters. The isotope compositions also revealed that the recharge elevations of the Hisaralan thermal waters were higher than those of the Emendere waters. In previous studies, Kocabaş et al. (2016) reported similar results for both the $\delta^{18}O$ and $\delta^{2}H$ compositions for the Hisaralan waters, although the $\delta^{18}O$ and $\delta^{2}H$ values given by Aksoy et al. (2009) were quite different than the current data.

4.2.2. Tritium compositions

The residence time (from infiltration to monitoring site) of natural waters is defined as the time that has elapsed since the water was in contact with the atmosphere (Kralik, 2015). The radioactive ^{3}H isotope is the most common tool to estimate this time interval. The ^{3}H concentration in the atmosphere was about 25 TU prior to 1953, but by the beginning of nuclear testing, the concentration had increased up to 2200 TU (Faure, 1986).

The ^{3}H values of the Hisaralan waters (thermal + cold) varied in a broad range, from 0 to 4.62 TU (Table 3). The ^{3}H composition of the thermal waters ranged from 0 to 0.72 TU in April to 0.01 to 0.54 TU in October. The low ^{3}H values of the thermal waters indicated a residence time of over 50 years. The cold waters were represented by higher ^{3}H values, which ranged from 2.64 to 2.82 TU to 2.82 to 4.62 TU for the respective periods, implying that they were diluted to varying extents by the meteoric fluids in the wet season. Regarding the Emendere field, which was sampled in October 2017, the thermal waters had a ^{3}H composition in the range of 0 to 1.33 TU and the cold waters (Emendere cold spring) had a ^{3}H value of 3.44 TU (Table 3). The ^{3}H concentration of the Emendere waters

indicated a contribution from younger waters (except for sample EM-4). The ^{3}H composition of the rainwater in the Hisaralan area was in the range of 3.72 to 8.21 TU (average 5.69 TU), and that of the snowfall was 7.34 TU. It was clear that the rainfall had higher ^{3}H values than the thermal waters, indicating that the cold waters were significantly contributed to by young rainfall.

4.2.3. Carbon isotopes

Carbon in the waters could have originated from a number of sources, which include limestone, mantle, organic material, and the atmosphere. The isotope composition of these carbon reservoirs varied in a wide range, from –30‰ for coal to 0‰ for the marine limestone, and even up to 10‰ for metamorphic CO_2 (Clark and Fritz, 1997). The $\delta^{13}C$ composition of DIC in the samples fell in the range of –4.33‰ to –2.77‰ (VPDB) for the thermal waters and varied from –13.84‰ to –12.51‰ (VPDB) for the cold waters (Table 3). Regarding the previous studies of geothermal fluids from the Balıkesir region, the reported $\delta^{13}C$ values for the Hisaralan area (–4.8‰ to –3.4‰; Mutlu, 2007) were within the range of the studied thermal waters.

4.2.4. Sulfur and oxygen isotopes of the dissolved sulfate

In natural waters, $\delta^{34}S$ values fell in a wide range, from –50‰ to +50‰ due to the various oxidation states of the sulfur (–2 to 6) (Krouse and Mayer, 2000; Izbicki et al., 2005) and therefore, the source of the sulfate in thermal waters was highly variable. The $\delta^{34}S$ composition of the dissolved sulfate in the Hisaralan geothermal samples varied from 13.17‰ to 15.97‰ (VCDT) and the $\delta^{18}O$ values were between –1.58‰ and 1.33‰ (VSMOW) (Table 3). In a previous study by Mutlu (2007), the $\delta^{34}S$ values of the Hisaralan waters were reported as 15.5‰ to 17.0‰, which fell in the range obtained herein.

5. Discussion

5.1. Major ion chemistry

The chemical composition of geothermal waters is extremely variable and chiefly depends on the geochemistry of the reservoir rocks. The Na-HCO_3 character of the Hisaralan thermal waters might have been due to the dissolution of feldspar minerals in the volcanic rocks by the following reactions, which released either kaolinite or gibbsite as the clay residue:

$$2NaAlSi_3O_8 + 2CO_2 + 3H_2O \leftrightarrow 2Na^+ + 2HCO_3^- + 4SiO_2 + Al_2Si_2O_5(OH)_4 \text{ (kaolinite)} \quad (1)$$

$$NaAlSi_3O_8 + CO_2 + 2H_2O \leftrightarrow Na^+ + HCO_3^- + 3SiO_2 + Al(OH)_3 \text{ (gibbsite)} \quad (2)$$

Dissolution of K involves a similar process to that of sodium. On the other hand, Ca-HCO_3-type cold waters probably owe their nature to the dissolution of Ca-plagioclase or calcite, which requires high P_{CO2}.

$$CaAl_2Si_2O_8 + 2CO_2 + 3H_2O \leftrightarrow Ca^{2+} + 2HCO_3 + Al_2Si_2O_5(OH)_4 \quad (3)$$

$$CaAl_2Si_2O_8 + 2CO_2 + 4H_2O \leftrightarrow Ca^{2+} + 2HCO_3 + 2SiO_2 + 2Al(OH)_3 \quad (4)$$

$$CaCO_3 + CO_2 + H_2O \leftrightarrow Ca^{2+} + 2HCO_3 \quad (5)$$

In Figure 5, concentrations of the major ions and temperatures of waters sampled in both periods are plotted against their Cl content. Cl showed strong positive correlations with the Na, K, HCO_3, SO_4, SiO_2, B, and Li concentrations. The Ca and Mg contents of the waters did not display any significant correlation with Cl, which was possibly attributed to the dissolution and/or precipitation of the carbonate minerals (e.g., calcite). Relatively moderate B (3.4 to 6.6 mg/L) and Li (0.7 to 1.3 mg/L) concentrations in the Hisaralan thermal waters might be explained by a simple rock leaching process. It was noticeable that the SiO_2, B, and Li concentrations of the waters sampled in October were higher than those in April, although the Cl contents of the samples in both seasons remained almost unchanged (Figure 5).

5.2. Mineral saturation

Mineral saturation tendencies provide awareness of scaling problems that were encountered during drilling, particularly in the production and transfer of thermal water from the wells, and management of the hot springs. Therefore, predicting the type of scaling in geothermal waters may greatly reduce operating costs. Calcite and aragonite, and to a lesser extent, quartz, are the most common scaling types that have been documented for Turkish geothermal waters (Mutlu and Güleç, 1998; Tarcan, 2005).

In this section, the saturation states of major carbonate (calcite, aragonite, dolomite, and strontianite), sulfate (anhydrite, gypsum, barite, and celestite), and silica/silicate (chalcedony, quartz, K-feldspar, K-mica, kaolinite, and sepiolite) minerals and fluorite were predicted, which had possibly precipitated from the Hisaralan and Emendere thermal waters. Saturation indices of these minerals were computed at the discharge temperatures of waters using the PhreeqCi program (Parkhurst and Appelo, 1999) and the results are given in Table 4, where positive values stand for oversaturation, while negative values represent undersaturation, and values at or close to zero (log SI = 0) indicate equilibrium between the water and minerals.

The saturation tendencies of most of the waters from both fields did not indicate seasonal changes, although the level of saturation may have changed to some extent. The results of the calculations showed that most of the Hisaralan thermal waters were saturated with respect

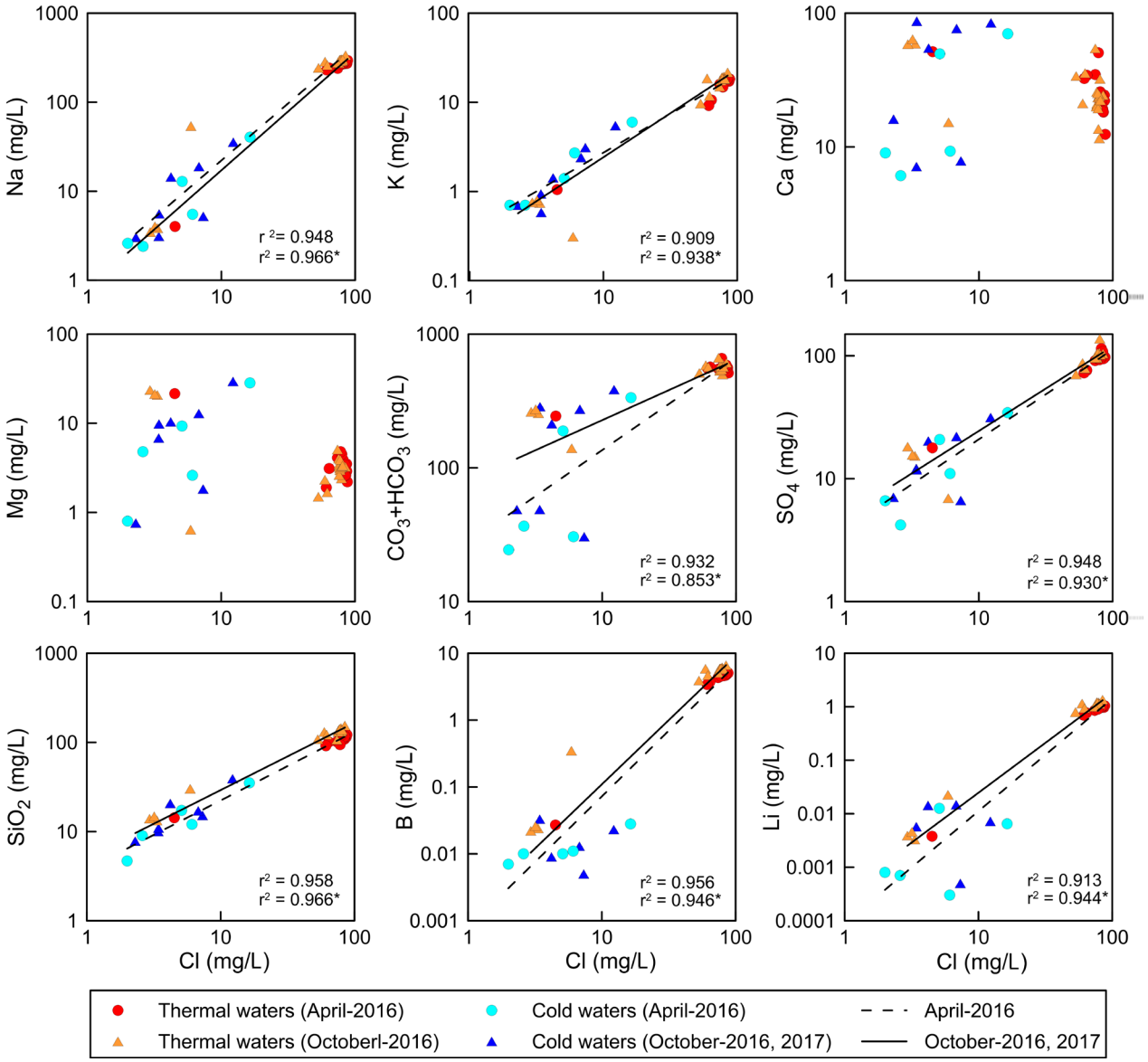

Figure 5. Diagram displaying chloride vs. other major ions, elements, and SiO_2 of the Hisaralan and Emendere waters (r*: October 2016, 2017).

to carbonate minerals, such as calcite, aragonite, and dolomite, which suggested that scaling of these minerals will cause a significant problem in the exploitation of the thermal waters. Saturation index values of chalcedony and quartz were slightly positive and very close to equilibrium (Table 4). This was supported by the results of the X-ray diffraction analysis of the samples collected from encrusted pipes in the Hisaralan geothermal area, which showed that calcite and aragonite were the chief minerals, accompanied by trace amounts of quartz. On the other hand, all of the sulfate phases displayed under saturation trends. Regarding the Emendere geothermal area, the waters were undersaturated with respect to most of the minerals as the result of their low TDS contents.

5.3. Estimation of reservoir temperatures

5.3.1. Chemical geothermometers

Silica geothermometers are based on the experimentally determined solubility of various silica phases as a function of temperature. Pressure is generally assumed to be constant, since precipitation occurs at relatively shallow depths. The quartz geothermometer has been reported to yield better results for reservoir temperatures of >180 °C (Giggenbach, 1991). However, at lower temperatures,

Table 4. Saturation states of the Hisaralan waters with respect to certain minerals.

Sample No.		HSW	HS-1	HS-21	HS-26	HS-27	HS-40	HS-44	HS-46	HS-51	HS-54	HS-55	HS-56	HS-57	HS-58	HS-60	HS-61	HS-67	HS-68	HS-69	EM-1	EM-2	EM-3	EM-4
Measured temperature (°C)		97.0	93.2	85.6	97.0	74.0	73.6	95.1	93.0	95.7	75.1	-	-	87.9	78.0	77.6	96.4	54.1	69.8	54.5	-	-	31.0	-
April 2016	Anhydrite	−1.68	−1.69	−1.80	−2.01	−1.89	−1.91	−1.82	−1.77	−1.72	−1.76	-	-	−1.74	−1.90	−1.95	−1.64	−1.87	−1.90	−2.11	-	-	−2.69	-
	Aragonite	0.89	0.30	0.36	0.93	0.20	0.18	0.81	0.41	0.41	0.13	-	-	0.11	0.20	0.17	0.51	0.05	0.18	−0.11	-	-	−0.08	-
	Barite	−0.19	−0.18	−0.17	−0.29	−0.07	−0.10	−0.25	−0.22	−0.27	−0.10	-	-	−0.11	−0.09	−0.07	−0.24	−0.04	−0.07	0.07	-	-	−0.30	-
	Calcite	1.00	0.40	0.46	1.03	0.31	0.29	0.91	0.51	0.51	0.24	-	-	0.21	0.31	0.28	0.62	0.18	0.29	0.01	-	-	0.06	-
	Celestite	−2.02	−2.02	−1.96	−2.03	−1.95	−1.96	−1.98	−1.98	−1.97	−1.93	-	-	−1.89	−1.93	−1.92	−2.00	−1.85	−1.96	−1.96	-	-	−3.02	-
	Chalcedony	0.15	0.16	0.24	0.14	0.34	0.33	0.16	0.18	0.16	0.28	-	-	0.22	0.29	0.32	0.18	0.44	0.32	0.42	-	-	−0.14	-
	Dolomite	1.31	0.10	0.33	1.54	0.14	0.13	1.17	0.34	0.41	−0.05	-	-	−0.14	0.23	0.19	0.63	−0.16	−0.01	−0.71	-	-	0.15	-
	Fluorite	−0.20	−0.19	−0.12	−0.53	−0.02	−0.05	−0.32	−0.19	−0.25	−0.04	-	-	−0.22	−0.17	−0.21	−0.18	0.03	−0.20	−0.17	-	-	−2.40	-
	Gypsum	−2.06	−2.04	−2.08	−2.40	−2.07	−2.09	−2.19	−2.12	−2.09	−1.95	-	-	−2.05	−2.12	−2.16	−2.02	−1.86	−2.04	−2.11	-	-	−2.45	-
	K-feldspar	−1.44	−1.78	−1.42	−1.86	−0.78	−0.65	−1.74	−1.00	−1.95	−0.87	-	-	−1.26	−1.17	−0.64	−1.59	−0.09	−1.05	−0.20	-	-	−2.54	-
	K-mica	1.14	1.19	1.40	−1.03	2.93	3.38	−0.04	2.99	0.51	3.55	-	-	2.59	2.02	3.33	1.39	5.07	2.88	5.10	-	-	2.64	-
	Kaolinite	−1.63	−1.19	−1.11	−3.42	0.07	0.36	−2.48	−0.13	−1.73	0.64	-	-	−0.16	−0.58	0.25	−1.17	1.88	0.29	1.99	-	-	0.92	-
	Quartz	0.40	0.42	0.52	0.39	0.64	0.62	0.42	0.44	0.41	0.58	-	-	0.49	0.58	0.61	0.43	0.79	0.63	0.77	-	-	0.27	-
	Sepiolite	−0.46	−2.87	−2.26	1.10	−2.77	−2.72	−0.28	−2.22	−2.25	−3.55	-	-	−3.29	−2.55	−2.43	−1.87	−4.04	−3.46	−4.59	-	-	−3.61	-
	Strontianite	−0.61	−1.22	−1.03	−0.25	−1.15	−1.16	−0.53	−0.98	−1.02	−1.32	-	-	−1.26	−1.10	−1.08	−1.01	−1.31	−1.19	−1.34	-	-	−1.86	-
Measured temperature (°C)		98.9	94	85.8	96.4	80.2	74.9	96.3	93.1	96.4	88.1	85.0	93.1	85.1	84.1	-	95.7	54.7	70.4	59.3	30.5	28.5	32.0	25.2
October 2016	Anhydrite	−1.63	−1.65	−1.78	−2.00	−1.81	−1.91	−1.72	−1.65	−1.69	−1.79	−1.88	−1.97	−1.54	−1.84	-	−1.68	−1.83	−1.86	−2.05	−2.71	−2.67	−2.66	−3.57
	Aragonite	0.89	0.57	0.50	0.86	0.32	0.54	0.59	0.48	0.51	0.21	0.45	0.80	0.62	−0.53	-	0.63	0.05	0.34	0.57	−0.26	0.76	0.06	0.63
	Barite	−0.09	−0.13	−0.14	−0.18	−0.06	−0.08	−0.19	−0.10	−0.19	−0.17	−0.15	−0.22	−0.05	−0.11	-	−0.19	−0.09	0.00	0.04	−0.43	−0.32	−0.38	−1.43
	Calcite	0.99	0.67	0.61	0.96	0.43	0.65	0.69	0.58	0.61	0.32	0.56	0.90	0.73	−0.42	-	0.73	0.17	0.46	0.69	−0.12	0.90	0.20	0.77
	Celestite	−1.90	−1.95	−1.92	−1.92	−1.87	−1.92	−1.94	−1.89	−1.91	−1.93	−2.05	−2.03	−1.79	−1.90	-	−1.92	−1.83	−1.85	−1.88	−3.14	−3.04	−3.10	−4.44
	Chalcedony	0.26	0.23	0.31	0.22	0.36	0.39	0.16	0.27	0.24	0.28	0.31	0.25	0.33	0.35	-	0.24	0.49	0.40	0.44	−0.17	−0.13	−0.14	0.20
	Dolomite	1.24	0.66	0.62	1.44	0.37	0.84	0.65	0.46	0.55	0.20	0.47	1.42	0.75	−1.24	-	0.81	−0.19	0.03	0.53	−0.29	1.81	0.35	0.50
	Fluorite	−0.31	−0.39	−0.38	−0.78	−0.30	−0.31	−0.48	−0.38	−0.48	−0.46	−0.40	−0.70	−0.28	−0.44	-	−0.47	−0.14	−0.40	−0.45	−2.31	−2.53	−2.33	−3.24
	Gypsum	−2.04	−2.01	−2.07	−2.38	−2.05	−2.10	−2.10	−2.00	−2.07	−2.10	−2.16	−2.32	−1.82	−2.12	-	−2.06	−1.83	−2.01	−2.10	−2.46	−2.41	−2.44	−3.27
	K-feldspar	−1.07	−1.03	−0.90	−1.13	−0.72	−0.35	−1.08	−0.81	−1.32	−1.19	−0.64	−0.87	−0.63	−0.59	-	−1.29	0.05	0.01	−0.16	−2.38	−2.35	−2.28	−1.09
	K-mica	1.51	2.54	2.32	0.68	2.81	3.18	2.60	3.08	1.69	2.12	3.12	1.67	3.02	4.90	-	1.49	5.27	5.21	3.74	4.11	1.75	3.60	2.91
	Kaolinite	−1.43	−0.45	−0.58	−2.26	−0.13	−0.02	−0.51	−0.05	−1.03	−0.57	−0.04	−1.45	−0.11	1.78	-	−1.24	2.04	1.71	0.59	2.19	−0.12	1.63	0.48
	Quartz	0.51	0.49	0.59	0.47	0.64	0.69	0.41	0.53	0.49	0.55	0.58	0.50	0.60	0.63	-	0.49	0.83	0.71	0.78	0.25	0.28	0.27	0.63
	Sepiolite	−0.25	−1.67	−1.64	1.20	−2.12	−1.18	−1.57	−1.98	−1.69	−2.28	−1.92	0.74	−1.54	−5.14	-	−1.16	−4.02	−3.15	−1.86	−4.74	−0.36	−3.56	0.26
	Strontianite	−0.53	−0.91	−0.87	−0.23	−0.99	−0.76	−0.80	−0.95	−0.88	−1.14	−0.95	−0.45	−0.86	−1.82	-	−0.78	−1.33	−0.95	−0.61	−2.14	−1.05	−1.81	−1.69

silica solubility is mostly controlled by chalcedony, and even cristobalite or amorphous silica at much lower temperatures. Results of silica geothermometers applied to the Hisaralan and Emendere geothermal waters are shown in Table 5. The chalcedony geothermometer (Fournier, 1977) yielded reservoir temperatures that ranged from 105 to 140 °C for the Hisaralan samples and 48 °C for those from Emendere (EM-4). The quartz, with the maximum and no-steam loss geothermometers of Fournier (1977), estimated higher results, which ranged from 129 to 163 °C, to 49 to 83 °C for the waters of the respective fields.

The cation geothermometers, unlike the silica geothermometers, are derived from concentration ratios rather than solubility of a single mineral. As a first approach, the Hisaralan and Emendere geothermal waters were plotted on the Na-K-Mg diagram of Giggenbach (1988) (Figure 6). The Emendere samples fell in the Mg corner, which is characteristic of shallow or mixed waters, whereas the Hisaralan samples fell into the boundary between the immature and partially equilibrated water fields. It was clear that none of the samples attained water-rock equilibrium and, therefore, it is suggested that the results of cation geothermometers should be interpreted cautiously and will not be discussed further.

5.3.2. Sulfate-water isotopic geothermometer

Reservoir temperatures of the selected waters (sampled in October) from the Hisaralan field were predicted using the $\delta^{18}O$ values of sulfate and water (Lloyd, 1968). The results yielded a temperature range of 179 to 224 °C (Table 5), which was notably higher than those estimated by the silica geothermometers. The difference was attributed to mixing of the geothermal waters with sulfate-rich waters or the slower rate of isotopic equilibrium between the sulfate and water, which possibly modified the oxygen isotopic composition of the sulfate (Nuti, 1991; Mutlu et al., 2012).

Table 5. Reservoir temperatures (°C) of the Hisaralan and Emendere waters.

No	April 2016				October 2016, 2017				
	T_{meas}	Chal[1]	Q_{MSL}[1]	Q_{NSL}[1]	T_{meas}	Chal[1]	Q_{MSL}[1]	Q_{NSL}[1]	$^{18}O(SO_4\text{-}H_2O)$[2]
HSW	97.0	120	140	146	98.9	140	154	163	198
HS-1	93.2	116	137	142	94.0	128	146	153	
HS-21	85.6	119	139	145	85.8	130	148	155	
HS-26	97.0	123	142	148	96.4	135	151	159	203
HS-27	74.0	119	139	145	80.2	130	147	154	
HS-40	73.6	116	137	142	74.9	129	146	153	
HS-44	95.1	121	140	146	96.3	131	148	156	199
HS-46	93.0	119	139	144	93.1	132	149	157	
HS-51	95.7	118	139	144	96.4	131	148	156	
HS-54	75.1	111	133	138	88.1	128	146	153	
HS-55					85.0	128	146	153	
HS-56					93.1	132	149	157	
HS-57	87.9	118	138	144	85.1	132	148	156	224
HS-58	78.0	117	138	143	84.1	133	150	158	219
HS-60	77.6	120	140	146					
HS-61	96.4	122	142	148	95.7	131	148	156	216
HS-67	54.1	107	130	134	54.7	115	136	141	179
HS-68	69.8	111	133	138	70.4	123	142	149	199
HS-69	54.5	105	129	132	59.3	115	136	142	
EM-1					30.5	-	56	49	
EM-2					28.5	-	57	50	
EM-3	31.0	-	58	51	32.0	-	59	52	
EM-4					25.2	48	83	80	

[1]Fournier (1977), [2]Lloyd (1968); T_{meas}: measured temperature; Q_{MSL}: quartz maximum steam loss; Q_{NSL}: quartz no steam loss; -: lower than outlet temperature; blank: no data.

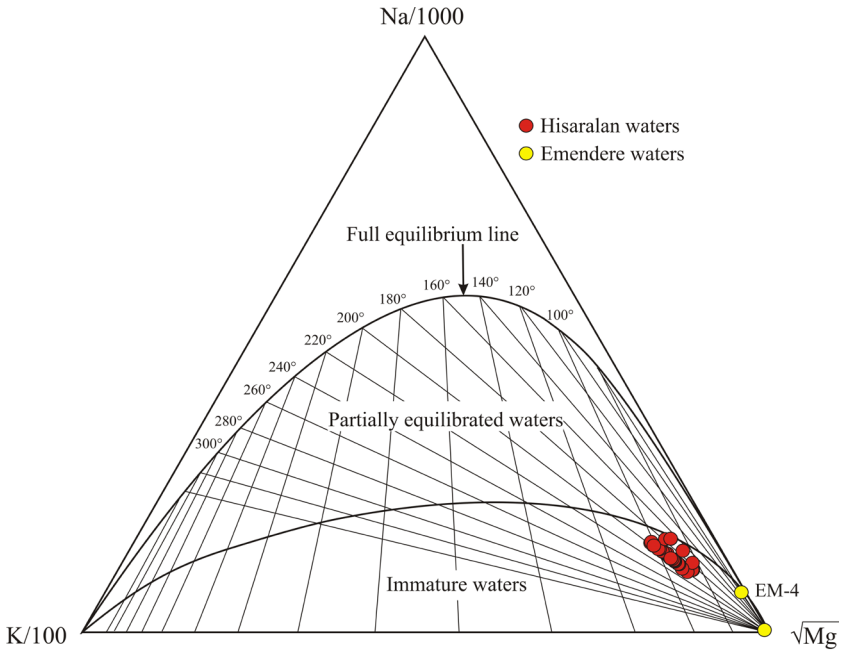

Figure 6. Na-K-Mg diagram for the Hisaralan and Emendere thermal waters.

5.3.3. Silica-enthalpy mixing model

The application of the silica-enthalpy model requires that silica was not deposited prior or subsequent to the mixing, because silica deposition results in an underestimation of temperature (Fournier, 1977). In this model, the silica concentrations and discharge temperatures of cold and mixed waters were used to determine the temperature of the hot-water component of the mixture, which possibly represented the reservoir temperature. In the silica-enthalpy diagram (Figure 7), enthalpy values of the Hisaralan samples that corresponded to the discharge temperatures were taken from the steam table given by Henley et al. (1984). For the prediction of the reservoir temperatures, it was assumed that steam separated before the mixing. Possible mixing curves were intersected on a vertical line projected upward from the boiling temperature of 100 °C (419 J/g), and the horizontal lines from these intersection points were connected to the quartz solubility (maximum steam loss) curve. The new points on this curve corresponded to reservoir temperatures of 146 °C for April and 154 °C for October (Figure 7). These values were quite consistent with the temperatures computed from the quartz geothermometer of the maximum steam loss.

5.3.4. Chloride-enthalpy mixing model

In the chloride-enthalpy diagram, the chloride contents (mg/L) and enthalpy values (kJ/g) (Henley et al., 1984), estimated from the measured temperatures of the Hisaralan cold and thermal waters (blue and red circles), were plotted (Figure 8). Next, each thermal water sample was connected with a boiling line to the steam point at 100 °C (0 mg/L chloride and 2775 J/g enthalpy). On these lines, temperatures computed by the quartz with

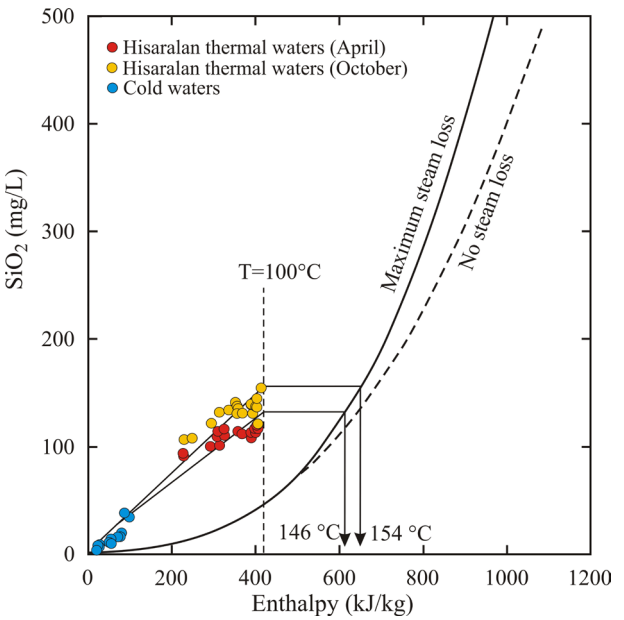

Figure 7. Silica-enthalpy diagram for the Hisaralan waters.

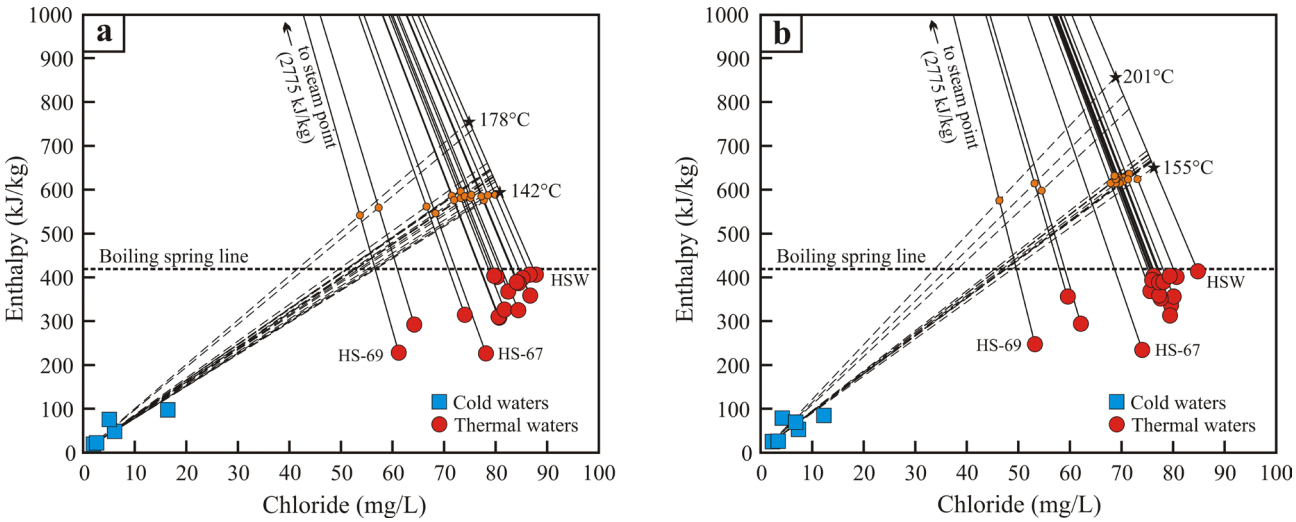

Figure 8. Chloride-enthalpy diagram for the Hisaralan waters sampled in a) April and b) October.

the steam loss geothermometer (orange circles) were marked. Possible mixing lines between these points and the cold waters coincided with the boiling lines at different positions (Figure 8). The new points at the boiling lines yielded reservoir temperatures ranging from 142 to 178 °C for 2016 and 155 to 201 °C for 2017. Geothermal wells drilled in the Simav Graben reached a depth of about 2500 m and ascertained bottom-hole temperatures over 180 °C (Gemici and Tarcan, 2002; Burçak et al., 2013). As recognised in the well log data, limestones of Bornova Flysch Zone and metamorphic rocks of the Menderes Massif comprise the secondary reservoirs at such depths (Okay et al., 2012), where fluids of higher temperature are produced.

5.4. Fluid source

Temperature, wind speed, atmospheric humidity, and evaporation of the recharge area exerted great control on the isotopic composition of precipitation and cold groundwaters, which resulted in deuterium excess in these waters. The deuterium excess was a function of the isotopic composition of oxygen ($\delta^{18}O$) and hydrogen ($\delta^{2}H$) in the water (d-excess = $\delta^{2}H - 8 \times \delta^{18}O$) (Dansgaard, 1964). The deuterium excess in meteoric water is greatly affected by the relative moisture originating from the evaporative source of the vapor (Pfahl and Sodemann, 2014; Uemura et al., 2008). Vapor derived from the eastern Mediterranean Sea is represented by a high d-excess value (>20‰), relative to the global average (~10‰). The d-excess values from the Aegean Sea vary from 13 to 17‰ (Gat and Carmi, 1970). Groundwaters in the Italian Alps (Cervi et al., 2017) and spring waters in Greece (Dotsika et al., 2018) have average d-excess of 12.5‰. In addition, d-excess values of groundwater in the central Italy were reported in the range of 9‰ to 21‰, reflecting recharge from the Mediterranean precipitation (Sappa et al., 2018). Likewise, the Hisaralan and Emendere waters had deuterium excess values between 12‰ and 18‰ (average 15.7‰), which were consistent with the range proposed for the Aegean Sea.

The $\delta^{2}H$ values of the studied thermal waters were much lower than those of the cold waters, which might have been attributed to recharge from meteoric waters that suffered from different climate regimes (e.g., more humid and cold conditions during the Pleistocene). Another alternative for the $\delta^{2}H$ shift was that steam separated from deep hot water and then condensation in the local groundwater at shallow depths. Positive change in $\delta^{2}H$ value is generally much less common than in $\delta^{18}O$, since most rocks contain little hydrogen relative to the water. However, in clay-dominated geothermal systems, deuterium exchange between water and hydrous clay minerals may occur to some extent, which may cause a change in the $\delta^{2}H$ (e.g., Ellis and Mahon, 1977). The upwelling zone of thermal waters in boreholes that opened through the epithermal veins around the Hisaralan area was dominated by smectite, mixed-layer illite-smectite- and illite-type minerals (Kocabaş et al., 2016). These clay minerals, via water-rock interaction processes, might have modified the d-excess value of the studied thermal waters.

Subsurface processes can modify the original isotopic values of geothermal waters. Isotopic exchange at high temperatures between the water and minerals may cause

an increase in the $\delta^{18}O$ composition of the water and a decrease in the $\delta^{18}O$ composition of the minerals. This eventually gives rise to an oxygen isotope shift in the $\delta^{18}O$-$\delta^{2}H$ diagram, towards more positive values of $\delta^{18}O$ (Ellis and Mahon, 1977). The degree of isotopic exchange depends on reservoir temperature, residence time of the water, and water-rock interaction. $\delta^{18}O$ values of the Hisaralan thermal waters deviated nearly 1‰ from the MaMWL line and 2‰ from the Eastern Mediterranean MWL, which might indicate that water-rock interaction processes occurred in a low to moderate enthalpy geothermal system. However, mixing of thermal water with cold groundwater during rise to the surface may also greatly decrease the initial $\delta^{18}O$ of thermal water.

The notable difference between the $\delta^{13}C$ values of the thermal and cold waters implied a different source for the dissolved carbon (Table 3). Indeed, the $\delta^{13}C$ values of the recrystallised limestones of the Bornova Flysch Zone in the southern Marmara region, which varied from –3.40‰ to 2.59‰ (Mutlu 2007), were consistent with those of the Hisaralan waters. As the $\delta^{13}C$ composition of the studied thermal waters was very close to that of marine limestone (–3‰ to 3‰; Clark and Fritz, 1997), dissolution of the carbonates was likely to be the sole mechanism behind the observed $\delta^{13}C$ values. However, the $\delta^{13}C$ of the cold waters, with relatively lower values, might indicate an organic source.

The $\delta^{13}C$ and $\delta^{18}O$ compositions of the travertine deposits in the Hisaralan area were reported as –2.97‰ to 0.07‰ (VPDB) and –10.00‰ to –6.12‰ (VSMOW), respectively (Mutlu, 2007). The relatively high $\delta^{13}C$ values of the travertines might be explained by preferential CO_2 degassing from fluids which, in turn, resulted in the depletion in light-isotopes (^{16}O and ^{12}C). Precipitation from such isotopically-enriched waters explains the isotopically heavy character of the Hisaralan travertines (Liu et al., 2003; Uysal et al., 2007; Özkul et al., 2014; Karabacak et al., 2017). To test this, the equation of the oxygen isotope fractionation between calcite and water ($\Delta^{18}O_{calcite\text{-}water}$) was used (Friedman and O'Neil, 1977). The $\delta^{18}O$ values of fluids that precipitated travertines were computed using a temperature range of 55 to 95 °C (minimum and maximum measured temperatures of the springs) and the $\delta^{18}O$ values of the travertines varied from –10‰ to –6.12‰ (Mutlu, 2007). Assuming that the measured temperatures of fluids were likely the same at the time of the travertine deposition, the waters in equilibrium with calcite were found to have a $\delta^{18}O$ composition ($\delta^{18}O_{water}$) in the range of –8.0‰ to –4.1‰ (VSMOW) for 55 °C and 1.6‰ to 2.3‰ (VSMOW) for 95 °C. These values were within the range of meteoric waters, although positive values might have been due to the interaction of meteoric fluids with ^{18}O-enriched rocks at moderate temperatures (Coşanay et al., 2017). The $\delta^{18}O$ compositions of the clay samples collected from the boreholes that opened through the epithermal veins around the Hisaralan area were –0.9‰ to 7.2‰ (VSMOW) (Kocabaş et al., 2016). The $\delta^{18}O_{water}$ of the hydrothermal waters equilibrating with these clays at a temperature of 200 °C was estimated as –8‰ to –5‰ (VSMOW), which indicated that meteoric fluids exerted a great contribution to the formation of the clay minerals.

Carbon isotopes, unlike oxygen isotopes, cannot be used to estimate the equilibrium temperature; however, they may provide significant insight into the source rocks. As shown in Figure 9, the $\delta^{13}C$ of the samples increased with an increasing total DIC (TDIC) content, which was computed using the PhreeqC code (Parkhurst and Appelo, 1999). In this diagram, which was constructed using the theoretical $\delta^{13}C_{TDIC}$ curves computed by Chiodini et al. (2000), the evolution of the TDIC and the $\delta^{13}C$ composition of the waters were examined, assuming that no CO_2 degassing and thus, no calcite precipitation, had occurred. Considering that meteoric water penetrates through the carbonate terrain in the absence of deep CO_2 flux (Figure 9), the cold waters plotted a $\delta^{13}C_{TDIC}$ curve for a $\delta^{13}C_{bio}$ value of –26‰, which indicated a strong control of soil CO_2 on dissolution of the limestones. On the other hand, the thermal waters, with higher TDIC and $\delta^{13}C$ values, followed the trend of inorganic carbon input, which implied the contribution of deep geogenic CO_2.

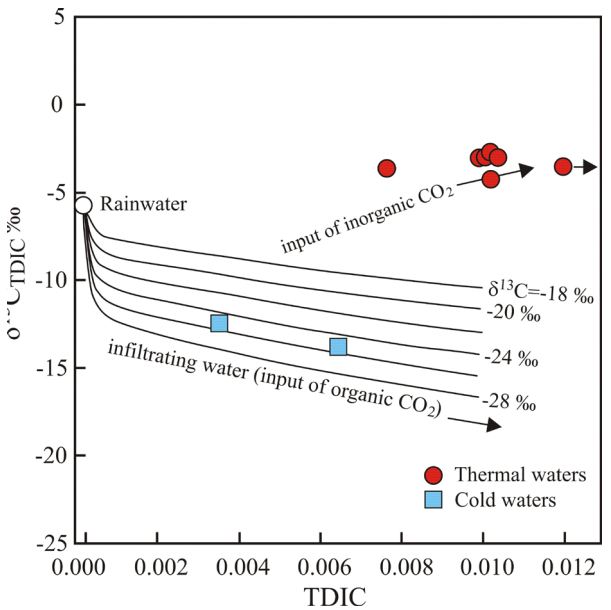

Figure 9. TDIC vs. $\delta^{13}C_{TDIC}$ diagram for the Hisaralan thermal and cold waters. Rainwater composition and theoretical curves representing groundwater infiltrating through carbonate terrains in the absence of deep CO_2 flux were from Chiodini et al. (2000).

In a previous study by Mutlu et al. (2008), the (mid-ocean ridge basalt) $^{3}He/^{4}He$ ratio of a gas sample collected from a bubbling spring in the Hisaralan site was reported as 0.66 Ra, which was greater than the crustal value (average $R/R_A = 0.05$; Andrews, 1985). This value yielded an 8% mantle contribution to the helium inventory of volatiles in the region. The $\delta^{13}C$ (CO_2) value of this spring was –8.04‰ (VPDB) (Mutlu et al., 2008), which was lower than the $\delta^{13}C$ (DIC) of the thermal waters, but higher than that of the cold waters. According to Karakuş (2015), the $^{3}He/^{4}He$ ratios of gas samples from the Simav geothermal field (Figure 1a), in the eastern realm of the Simav Graben, were in the range of 1.03 to 1.57 Ra, which indicated a mantle contribution of 16.8% to 19.4%. A quantitative assessment of the carbon inventory of the Hisaralan and Simav gas samples revealed that marine limestone was the major contributor to the carbon budget (68% to 80%), followed by sedimentary organic carbon (1% to 26%), and mantle CO_2 (1% to 32%) (Mutlu et al., 2008; Karakuş, 2015). This wide range estimated for the carbon provenance could have been attributed to isotope fractionation of the volatiles enroute to the surface. It was concluded that limestones within the Bornova Flysch Zone were the reservoir rocks of the Hisaralan geothermal fluids, which contained mantle-derived He and CO_2 gases to some extent.

The $\delta^{34}S$ values of the waters were far from the magmatic (0‰ ± 2‰) and organic (~ –30‰) ranges. However, the $\delta^{34}S$ and $\delta^{18}O$ systematics of the samples, which varied in a narrow range, were close to the array proposed for the nonmarine evaporites (–15‰ to 10‰ for $\delta^{34}S$ and –10‰ to 4‰ for $\delta^{18}O$; Clark and Fritz, 1997). The fact that the region hosted no evaporite deposits of either marine or terrestrial origin led to the proposal of an alternative source for the sulfur in the studied waters. As suggested by Kampschulte and Strauss (2004) and Mutlu et al. (2012), sedimentary carbonates might have significant sulfate concentrations of up to 24,000 ppm, and burial recrystallisation of these carbonates may have been a major sulfur source in the sedimentary basins. This process, called the structural substitution of sulfate (carbonate-associated sulfate) into carbonates, could have been a possible source of dissolved sulfate in the Hisaralan samples. It is important to note that the Hisaralan thermal waters had an intense rotten egg odor, probably due to presence of hydrogen sulfide (H_2S), which is thought to emanate through the active faults in the Hisaralan area (either magmatic or biogenic origin). However, this argument could not be tested, since S isotope data on H_2S were not available.

5.5. Constraints on water circulation

The ^{3}H radioactive isotope of hydrogen has a half-life of 12.32 years. Since ^{3}H is a part of the water molecule, like other isotopes of hydrogen (e.g., ^{2}H and ^{1}H), it is regarded as an ideal tracer. Chloride that behaves in a relatively conservative manner is also used as a tracer in hydrogeological studies. In the Cl vs. ^{3}H diagram (Figure 10a), the thermal and cold waters (sampled on October

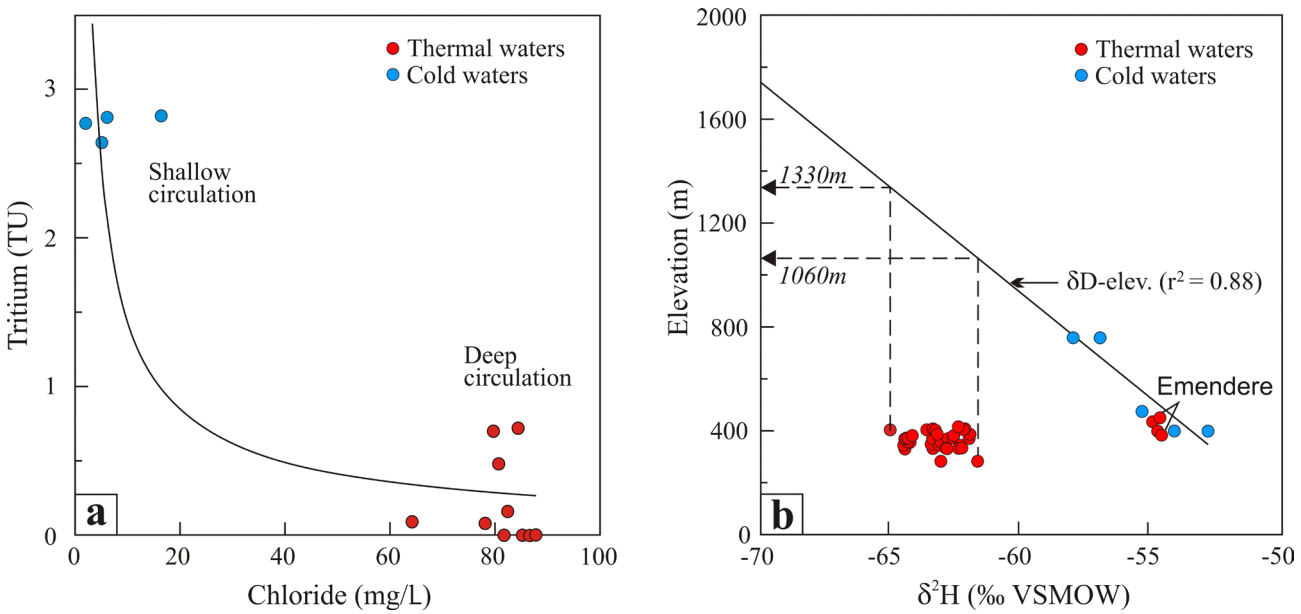

Figure 10. a) Cl vs. ^{3}H diagram for the studied waters (April). b) $\delta^{2}H$-elevation graphic for the Hisaralan waters.

2016) in the Hisaralan field were clustered in 2 distinct areas. Cold waters, with relatively high ^{3}H (2.6 to 2.8 TU) and low Cl (2 to 16 mg/L) contents, were plotted in the left upper part of the Cl-^{3}H diagram, whereas thermal waters, with low ^{3}H (0.05 to 0.7 TU) and moderately high Cl (62 to 88 mg/L) contents, were plotted at the right lower quadrant, which indicated a relatively deeper circulation and longer residence time.

Oxygen and hydrogen isotopes can be used to estimate the recharge elevation as long as their compositions remain unchanged or not fractionated along the flow path. Based on the fact that isotopic composition of precipitation varies with respect to altitude, the recharge area of a spring can be identified (Clark and Fritz, 1997). In previous studies, both oxygen and hydrogen isotope data were successfully applied for the identification of recharge zones (Giggenbach et al., 1983; James et al., 2000; Schürch et al., 2003). In Figure 10b, the $\delta^{2}H$ values of the Hisaralan cold and hot samples were plotted against their sampling elevation, assuming that the isotope compositions of the cold waters were comparable to the modern precipitation. Using the moderate correlation between the altitude and $\delta^{2}H$ (r^{2} = 0.88) of the Hisaralan cold waters, the recharge area of the thermal waters was found at elevations between 1060 and 1330 m. Ulus Mountain, which has an altitude of about 1770 m in the NE part of the study area (Figure 1b), is likely to be the ultimate recharge zone of the Hisaralan waters.

6. Conclusion

The Hisaralan area hosts one of the high-temperature geothermal fields in western Turkey. Hisaralan thermal waters, with discharge temperatures of 54 to 99 °C, are Na-HCO_3-type waters. The $\delta^{18}O$ and $\delta^{2}H$ values of the water samples fall between the GMWL and MaMWL. The $\delta^{18}O$ values of the fluids, which precipitated travertines in the Hisaralan area, were estimated in the range of –8.0‰ to 2.3‰ (VSMOW), which were closely consistent with values of meteoric waters. The $\delta^{13}C$ (DIC) points to the fact that the carbon in the thermal waters might be derived from dissolution marine carbonates, whereas the carbon in the cold waters likely originates from an organic source. The $\delta^{34}S$ systematics of the dissolved sulfate in the Hisaralan geothermal waters indicated that the sulfate is most likely derived from the dissolution of marine carbonates and terrestrial evaporite units.

Reservoir temperatures computed from the silica geothermometers varied in a wide range, from 123 to 152 °C, which closely resembled those estimated by the silica-enthalpy (146 to 154 °C) and chloride-enthalpy (142 to 178 °C) mixing models. Temperatures estimated by SO_4-H_2O isotope geothermometry were between 179 and 224 °C, and did were not generally in agreement with the reservoir temperatures computed by the chemical geothermometers. Discordant temperatures may have been due to mixing of the thermal waters with sulfate-rich waters or the slower rate of isotopic equilibrium between the sulfate and water, which possibly modified the $\delta^{18}O$ of the sulfate. Recharge altitudes of the thermal waters estimated from the $\delta^{2}H$ compositions were between 1060 and 1330 m. Since the chemical geothermometers yielded a reservoir temperature of around 150 °C, the thermal waters produced from deeper parts of the Hisaralan geothermal system could be utilised for electricity production. However, a special care should be given to travertine towers, which have been placed under protection.

Acknowledgments

This study was financially supported by the Scientific and Technological Research Council of Turkey (TÜBİTAK) under grant no. 115Y141. The authors wish to thank Ekrem Yavaş and Himmet Taşlıoğlu, from the Sındırgı Municipality, for their logistic support. Three anonymous referees are acknowledged for their helpful suggestions about the manuscript.

References

Akkuş İ, Akıllı H, Ceyhan S, Özçelik N (2005). Turkish Geothermal Resource Inventory. General Directorate of Mineral Research and Exploration, publication no. 201. Ankara, Turkey: General Directorate of Mineral Research and Exploration (in Turkish).

Aksoy N, Demirkıran Z, Şimşek C (2009). Assessment of geochemical characteristics of the Sındırgı–Hisaralan (Balıkesir) geothermal field. In: IX. National Installation Engineering Congress (TESKON), Geothermal Energy Seminar; İzmir, Turkey. pp. 61-72 (in Turkish with English abstract).

Andrews JN (1985). The isotopic composition of radiogenic He and its use to study groundwater movement in confined aquifer. Chemical Geology 49: 339-351. doi: 10.1016/0009-2541(85)90166-4

Atabey E (2000). Earthquake. General Directorate of Mineral Research and Exploration, Education series No. 34. Ankara, Turkey: General Directorate of Mineral Research and Exploration (in Turkish).

Baba A, Sözbilir H (2012). Source of arsenic based on geological and hydrogeochemical properties of geothermal systems in western Turkey. Chemical Geology 334: 364-377. doi: 10.1016/j.chemgeo.2012.06.006

Bilim F, Akay T, Aydemir A, Koşaroğlu S (2016). Curie point depth, heat-flow and radiogenic heat production deduced from the spectral analysis of the aeromagnetic data for geothermal investigation on the Menderes Massif and the Aegean Region, western Turkey. Geothermics 60: 44-57. doi: 10.1016/j.geothermics.2015.12.002

Brinkmann R (1971). Das kristalline Grundgebirge von Anatolien. Geologische Rundschau 60: 886-899 (in German with an abstract in English). doi: 10.1007/BF02046526

Bozkurt E (2003). Origin of NE-trending basins in western Turkey. Geodinamica Acta 16: 61-81. doi: 10.1016/S0985-3111(03)00002-0

Bundschuh J, Maity JP, Nath B, Baba A, Gündüz O et al. (2013). Naturally occurring arsenic in terrestrial geothermal systems of western Anatolia, Turkey: potential role in contamination of freshwater resources. Journal of Hazardous Materials 262: 951-959. doi: 10.1016/j.jhazmat.2013.01.039

Burçak M, Dünya H, Hacısalihoğlu Ö (2013). New approaches on the investigation of covered geothermal fields: exploration of Kütahya-Şaphane-Karaca derbent buried geothermal fields and their developments. Bulletin of Mineral Research and Exploration 147: 127-151.

Cervi F, Borgatti L, Dreossi G, Marcato G, Michelini M et al. (2017). Isotopic features of precipitation and groundwater from the Eastern Alps of Italy: results from the Mt. Tinisa hydrogeological system. Environmental Earth Sciences 76: 410. doi: 10.1007/s12665-017-6748-9

Clark I, Fritz P (1997). Environmental Isotopes in Hydrogeology. New York, NY, USA: Lewis Publishers.

Chiodini G, Frondini F, Cardellini C, Parello F, Peruzzi L (2000). Rate of diffuse carbon dioxide Earth degassing estimated from carbon balance of regional aquifers: the case of central Apennine, Italy. Journal of Geophysical Research 105 (B4): 8423-8434. doi: 10.1029/1999JB900355

Craig H (1961). Isotopic variation in meteoric waters. Science 133: 1702-1703. doi: 10.1126/science.133.3465.1702

Coşanay P, Varol E, Çevik N, Kızılkanat C, Mutlu H et al. (2017). Geochemical, microthermometric and isotopic constraints on the origin of fluorite deposits in central Anatolia, Turkey. Turkish Journal of Earth Sciences 26 (3): 206-226. doi: 10.3906/yer-1701-1713.

Çemen İ, Catlos EJ, Göğüş O, Özerdem C (2006). Postcollisional extensional tectonics and exhumation of the Menderes Massif in Western Anatolia extended terrane, Turkey. In: Dilek Y, Pavlides S (editors). Postcollisional Tectonics and Magmatism in the Mediterranean Region and Asia. Geological Society of America, Special Papers 409: 353-379. doi: 10.1130/2006.2409(18)

Dansgaard W (1964). Stable isotopes in precipitation. Tellus 16 (4): 436-468. doi: 10.1111/j.2153-3490.1964.tb00181.x

Dotsika E, Diamantopoulos G, Lykoudis S, Poutoukis D, Kranioti E (2018). Isotopic composition of spring water in Greece: spring waters isoscapes. Geosciences 8: 238. doi: 10.3390/geosciences8070238

Ece Ö, Ekinci B, Schroeder PA, Crowe D, Esenli F (2013). Origin of the Düvertepe kaolin–alunite deposits in Simav Graben, Turkey: timing and styles of hydrothermal mineralization. Journal of Volcanology and Geothermal Researches 225: 57-78. doi: 10.1016/j.jvolgeores.2013.01.012

Ellis AJ, Mahon WAJ (1977). Chemistry and geothermal systems. New York, NY, USA: Academic Press.

Emre Ö, Doğan A, Özalp S (2011). 1:250.000 scale active fault map series of Turkey, Balıkesir (NJ 35-3) Quadrangle. Serial number: 4, General Directorate of Mineral Research and Exploration. Ankara, Turkey; General Directorate of Mineral Research and Exploration.

Erdoğan B, Güngör T (1992). Stratigraphy and tectonic evolution of the northern margin of the Menderes Massif. Turkish Association of Petroleum Geologists Bulletin 4: 9-34.

Erkül F, Helvacı C, Sözbilir H (2005). Stratigraphy and geochronology of the Early Miocene volcanic units in the Bigadiç borate basin, Western Turkey. Turkish Journal of Earth Sciences 14 (3): 227-253.

Erkül F, Helvacı C, Sözbilir H (2006). Olivine basalt and trachyandesite peperites formed at the subsurface/surface interface of a semi-arid lake: an example from the Early Miocene Bigadic¸ basin, western Turkey. Journal of Volcanology and Geothermal Researches 149: 240-262. doi: 10.1016/j.jvolgeores.2005.07.016

Ersoy EY, Çemen İ, Helvacı C, Billor Z (2014). Tectono-stratigraphy of the Neogene basins in Western Turkey: implications for tectonic evolution of the Aegean Extended Region. Tectonophysics 635: 33-58. doi: 10.1016/j.tecto.2014.09.002

Faure G (1986). Principles of Isotope Geology. 2nd ed. New York, USA: John Wiley and Sons Inc.

Fournier RO (1977). Chemical geothermometers and mixing models for geothermal systems. Geothermics 5: 41-50. doi: 10.1016/0375-6505(77)90007-4

Friedman I, O'Neil JR (1977). Compilation of stable isotope fractionation factors of geochemical interest. Report, USGS Numbered Series. Washington, USA: U.S. Government Printing Office.

Gat JR, Carmi I (1970). Evolution of the isotopic composition of the atmospheric water in the Mediterranean Sea area. Journal of Geophysical Research 75: 3039-3048.

Gat JR, Carmi I (1987). Effect of climate changes on the precipitation patterns and isotopic composition of water in a climate transition zone: case of the Eastern Mediterranean Sea area. In Solomon SI, Beran M, Hogg W (editors). The Influence of Climate Change and Climatic Variability on the Hydrologie Regime and Water Resources. Oxfordshire, UK: IAHS Publication, pp. 501-513.

Gemici Ü, Tarcan G (2002). Hydrogeochemistry of the Simav geothermal field, western Anatolia, Turkey. Journal of Volcanology and Geothermal Researches 116: 215-233.

Gemici Ü, Tarcan G (2007). Hydrogeochemistry of the Hisarköy geothermal area (Balıkesir) Western Turkey. In: 12th International Symposium on Water-Rock Interaction; Kunming, China. pp. 203-206.

Giggenbach WF, Gonfiantini R, Jangi BL, Truesdell AH (1983). Isotopic and chemical composition of parbati valley geothermal discharges, North-West Himalaya, India. Geothermics 12: 192-222.

Giggenbach WF (1988). Geothermal solute equilibria: derivation of Na-K-Mg-Ca geoindicators. Geochimica Cosmochimica Acta 52: 2749-2765. doi: 10.1016/0016-7037(88)90143-3

Giggenbach WF (1991). Chemical techniques in geothermal exploration. In: D'amore F (coordinator). Application of Geochemistry in Geothermal Reservoir Development. New York, NY, USA: UNITAR, pp. 119-144.

Henley RW, Truesdell AH, Barton PB, Whitney JA (1984). Fluid–Mineral Equilibria in Hydrothermal Systems. Reviews in Economic Geology, Vol. 1. Littleton, CO, USA: Society of Economic Geologist, Inc.

İlkışık OM (1995). Regional heat flow in western Anatolia using silica temperature estimates from thermal springs. Tectonophysics 244: 175-184. doi: 10.1016/0040-1951(94)00226-Y

Izbicki JA, Christensen AH, Newhouse MW, Aiken GR (2005). Inorganic, isotopic, and organic composition of high-chloride water from wells in a coastal southern California aquifer. Applied Geochemistry 20: 1496-1517. doi: 10.1016/j.apgeochem.2005.04.010

James ER, Manga M, Rose TP, Hudson GB (2000). The use of temperature and the isotopes of O, H, C, and noble gases to determine the pattern and spatial extent of groundwater flow. Journal of Hydrology 237: 100-112. doi: 10.1016/S0022-1694(00)00303-6

Jolivet L, Faccenna C, Huet B, Labrousse L, Pourhiet L et al. (2013). Aegean tectonics: strain localisation, slabtearing and trench retreat. Tectonophysics 597-598: 1-33. doi: 10.1016/j.tecto.2012.06.011

Kampschulte A, Strauss H (2004). The sulfur isotopic evolution of Phanerozoic seawater based on the analysis of structurally substituted sulfate in carbonates. Chemical Geology 204: 255-286. doi: 10.1016/j.chemgeo.2003.11.013

Karabacak V, Uysal IT, Ünal-İmer E, Mutlu H, Zhao J (2017). U-Th evidence from carbonate veins for episodic crustal deformation of Central Anatolian Volcanic Province. Quaternary Science Reviews 177: 158-172. doi: 10.1016/j.quascirev.2017.10.022

Karakuş H (2015). Helium and carbon isotope composition of gas discharges in the Simav Geothermal Field, Turkey: implications for the heat source. Geothermics 57: 213-223. doi: 10.1016/j.geothermics.2015.07.005

Kocabaş C, Tokçaer M, Çolak M (2016). Clay mineralogy and geochemistry of fossil and active hydrothermal alteration in the Hisaralan Geothermal Field (Sındırgı-Balıkesir), western Turkey. Afyon Kocatepe University Journal of Science and Engineering 16: 132-154. doi: 10.5578/fmbd.10852

Konak N (2002). 1/500.000 scaled Turkish geology map, İzmir quadrangle.. Ankara, Turkey: General Directorate of Mineral Research and Exploration (in Turkish).

Kralik M (2015). How to estimate mean residence times of groundwater. Procedia Earth and Planetary Science 13: 301-306. doi: 10.1016/j.proeps.2015.07.070

Krouse HR, Mayer B (2000). Sulphur and oxygen isotopes in sulphate. In: Cook P, Herczeg AL (editors). Environmental tracers in subsurface hydrology. norwell, MA, USA: Kluwer Academic Publishers, pp. 195-231. doi: 10.1007/978-1-4615-4557-6_7

Lips ALW, Cassard D, Sözbilir H, Yılmaz H, Wijbrans JR (2001). Multistage exhumation of the Menderes Massif, Western Anatolia (Turkey). International Journal of Earth Sciences 89: 781-792. doi: 10.1007/s005310000101

Liu L, Suto Y, Bignall GN, Hashida T (2003). CO_2 injection to granite and sandstone in experimental rock/hot water systems. Energy Conversion and Management 44: 1399-1410. doi: 10.1016/S0196-8904(02)00160-7

Lloyd RM (1968). Oxygen isotope behavior in the sulfate–water system. Journal of Geophysical Research 73: 6099-6110. doi: 10.1029/JB073i018p06099

Mutlu H (2007). Constraints on the origin of the Balıkesir thermal waters (Turkey) from stable isotope ($\delta^{18}O$, δD, $\delta^{13}C$, $\delta^{34}S$) and major-trace element compositions. Turkish Journal of Earth Sciences 16: 13-32.

Mutlu H, Güleç N (1998). Hydrogeochemical outline of thermal waters and geothermometry applications in Anatolia, Turkey. Journal of Volcanology and Geothermal Researches 85: 495-515. doi: 10.1016/S0377-0273(98)00068-7

Mutlu H, Sarıız K, Kadir S (2005). Geochemistry and origin of the Şaphane alunite deposit, Western Anatolia, Turkey. Ore Geology Reviews 26: 39-50. doi: 10.1016/j.oregeorev.2004.12.003

Mutlu H, Güleç N, Hilton DR (2008). Helium-carbon relationships in geothermal fluids of western Anatolia, Turkey. Chemical Geology 247: 305-321. doi: 10.1016/j.chemgeo.2007.10.021

Mutlu H, Güleç N, Hilton DR, Aydın H, Halldórsson SA (2012). Spatial variations in gas and stable isotope compositions of thermal fluids around Lake Van: implications for crust-mantle dynamics in eastern Turkey. Chemical Geology 300-301: 165-176. doi: 10.1016/j.chemgeo.2012.01.026

Nuti S (1991). Isotope techniques in geothermal studies. In: D'amore F (coordinator). Application of geochemistry in geothermal reservoir development. New York, NY, USA: UNITAR, pp. 215-251.

Okay AI, Altıner D (2007). A condensed Mesozoic section in the Bornova Flysch zone: a fragment of the Anatolide–Tauride carbonate platform. Turkish Journal of Earth Sciences 16: 257-279.

Okay Aİ, İşintek İ, Altıner D, Özkan-Altıner S, Okay N (2012). An olistostrome-mélange belt formed along a suture: Bornova Flysch zone, western Turkey. Tectonophysics 568-569: 282-295. doi: 10.1016/j.tecto.2012.01.007

Oygür V (1997). Anatomy of an epithermal mineralization: Mumcu (Balıkesir–Sındırgı), inner-western Anatolia, Turkey. Bulletin of Mineral Research and Exploration 119: 29-39.

Özkul M, Gökgöz A, Kele S, Baykara MO, Shen C-C et al. (2014). Sedimentological and geochemical characteristics of a fluvial travertine: a case from the eastern Mediterranean region. Sedimentology 61: 291-318. doi: 10.1111/sed.12095

Parkhurst DL, Appelo CAJ (1999). User's guide to PHREEQC (version 2) – a computer program for speciation, batch-reaction, one-dimensional transport, and inverse geochemical calculations. US Geological Survey Water-Resources Investigations Report 99-4259.

Pfahl S, Sodemann H (2014). What controls deuterium excess in global precipitation? Climate of the Past 10: 771-781. doi: 10.5194/cp-10-771-2014

Sappa G, Vitale S, Ferranti F (2018). Identifying Karst aquifer recharge areas using environmental isotopes: a case study in central Italy. Geosciences 8: 351. doi: 10.3390/geosciences8090351

Seyitoğlu G, Scott BC (1994). Late Cenozoic basin development in West Turkey: Gördes basin: tectonics and sedimentation. Geological Magazine 131: 631-637. doi: 10.1017/S0016756800012425

Seyitoğlu G (1997a). The Simav Graben: an example of young E-W trending structures in the Late Cenozoic extensional system of western Turkey. Turkish Journal of Earth Sciences 6: 135-141.

Seyitoğlu G (1997b). Late Cenozoic tectono-sedimentary development of the Selendi and Uşak-Güre basins: a contribution to the discussion on the development of east-west and north-trending basins in western Turkey. Geological Magazine 134: 163-175. doi: 10.1017/S0016756897006705

Seyitoğlu G, Işık V, Çemen İ (2004). Complete Tertiary exhumation history of Menderes massif, western Turkey: a working hypothesis Turkey. Terra Nova 16: 358-364. doi: 10.1111/j.1365-3121.2004.00574.x

Schürch M, Kozel R, Schotterer U, Tripet J-P (2003). Observation of isotopes in the water cycle—the Swiss National Network (NISOT). Environmental Geology 45: 1-11.

Tarcan G (2005). Mineral saturation and scaling tendencies of waters discharged from wells (> 150 degrees C) in geothermal areas of Turkey. Journal of Volcanology and Geothermal Researches 142: 263-283. doi: 10.1016/j.jvolgeores.2004.11.007

Uemura R, Matsui Y, Yoshimura K, Motoyama H, Yoshida N (2008). Evidence of deuterium excess in water vapor as an indicator of ocean surface conditions. Journal of Geophysical Research 113. doi: 10.1029/2008JD010209

Uysal IT, Feng Y, Zhao J-X, Altunel E, Weatherley D et al. (2007). U-series dating and geochemical tracing of late quaternary travertine in coseismic fissures. Earth and Planetary Science Letters 257: 450-462. doi: 10.1016/j.epsl.2007.03.004

Van Hinsbergen DJJ (2010). A key extensional metamorphic complex reviewed and restored: the Menderes Massif of western Turkey. Earth-Science Reviews 102: 60-76. doi: 10.1016/j.earscirev.2010.05.005

Yalçın T (2007). Geochemical characterization of the Biga Peninsula thermal waters (NW Turkey). Aquatic Geochemistry 13: 75-93. doi: 10.1007/s10498-006-9008-2

Yılmaz Y, Genç ŞC, Gürer F, Bozcu M, Yılmaz K et al. (2000). When did the western Anatolian grabens begin to develop? In: Bozkurt E, Winchester JA, Piper JAD (editors). Tectonics and magmatism in Turkey and the surrounding area. Geological Society, London, Special Publications 173 (1): 353-384. doi: 10.1144/GSL.SP.2000.173.01.17

Yılmaz H, Sönmez NF, Akay E, Şener AK, Tufan ST (2013). Low-sulfidation epithermal Au-Ag mineralization in the Sındırgı District, Balıkesir Province, Turkey. Turkish Journal of Earth Sciences 22: 485-522. doi: 10.3906/yer-1204-10